CFHTLenS: higher order galaxy-mass correlations probed by galaxy-galaxy-galaxy lensing

P. Simon, T. Erben, P. Schneider, C. Heymans, H. Hildebrandt, H. Hoekstra, T. D. Kitching, Y. Mellier, L. Miller, L. van Waerbeke, et al.

Monthly Notices
of the
ROYAL ASTRONOMICAL SOCIETY

MNRAS **430,** 2476–2498 (2013) doi:10.1093/mnras/stt069

CFHTLenS: higher order galaxy–mass correlations probed by galaxy–galaxy–galaxy lensing

P. Simon,[1⋆] T. Erben,[1] P. Schneider,[1] C. Heymans,[2] H. Hildebrandt,[1,3] H. Hoekstra,[4,5] T. D. Kitching,[2] Y. Mellier,[6] L. Miller,[7] L. Van Waerbeke,[3] C. Bonnett,[8] J. Coupon,[9] L. Fu,[10] M. J. Hudson,[11,12] K. Kuijken,[4] B. T. P. Rowe,[13,14] T. Schrabback,[1,4,15] E. Semboloni[4] and M. Velander[4,7]

[1]*Argelander Institute for Astronomy, University of Bonn, Auf dem Hügel 71, D-53121 Bonn, Germany*
[2]*Scottish Universities Physics Alliance, Institute for Astronomy, University of Edinburgh, Royal Observatory, Blackford Hill, Edinburgh EH9 3HJ, UK*
[3]*Department of Physics and Astronomy, University of British Columbia, 6224 Agricultural Road, Vancouver, V6T 1Z1 BC, Canada*
[4]*Leiden Observatory, Leiden University, Niels Bohrweg 2, NL-2333 CA Leiden, the Netherlands*
[5]*Department of Physics and Astronomy, University of Victoria, Victoria, BC V8P 5C2, Canada*
[6]*Institut d'Astrophysique de Paris, Universit Pierre et Marie Curie - Paris 6, 98 bis Boulevard Arago, F-75014 Paris, France*
[7]*Department of Physics, Oxford University, Keble Road, Oxford OX1 3RH, UK*
[8]*Institut de Ciencies de lEspai, CSIC/IEEC, F. de Ciencies, Torre C5 par-2, E-08193 Barcelona, Spain*
[9]*Institute of Astronomy and Astrophysics, Academia Sinica, PO Box 23-141, Taipei 10617, Taiwan*
[10]*Key Lab for Astrophysics, Shanghai Normal University, 100 Guilin Road, 200234 Shanghai, China*
[11]*Department of Physics and Astronomy, University of Waterloo, Waterloo, ON N2L 3G1, Canada*
[12]*Perimeter Institute for Theoretical Physics, 31 Caroline Street N, Waterloo, ON N2L 1Y5, Canada*
[13]*Department of Physics and Astronomy, University College London, Gower Street, London WC1E 6BT, UK*
[14]*California Institute of Technology, 1200 E California Boulevard, Pasadena CA 91125, USA*
[15]*Kavli Institute for Particle Astrophysics and Cosmology, Stanford University, 382 Via Pueblo Mall, Stanford, CA 94305-4060, USA*

Accepted 2013 January 9. Received 2013 January 9; in original form 2012 November 8

ABSTRACT

We present the first direct measurement of the galaxy–matter bispectrum as a function of galaxy luminosity, stellar mass and type of spectral energy distribution (SED). Our analysis uses a galaxy–galaxy–galaxy lensing technique (G3L), on angular scales between 9 arcsec and 50 arcmin, to quantify (i) the excess surface mass density around galaxy pairs (excess mass hereafter) and (ii) the excess shear–shear correlations around single galaxies, both of which yield a measure of two types of galaxy–matter bispectra. We apply our method to the state-of-the-art Canada–France–Hawaii Telescope Lensing Survey (CFHTLenS), spanning 154 square degrees. This survey allows us to detect a significant change of the bispectra with lens properties. Measurements for lens populations with distinct redshift distributions become comparable by a newly devised normalization technique. That will also aid future comparisons to other surveys or simulations. A significant dependence of the normalized G3L statistics on luminosity within $-23 \leq M_r \leq -18$ and stellar mass within $5 \times 10^9\,\mathrm{M}_\odot \leq M_* \leq 2 \times 10^{11}\,\mathrm{M}_\odot$ is found ($h = 0.73$). Both bispectra exhibit a stronger signal for more luminous lenses or those with higher stellar mass (up to a factor of 2–3). This is accompanied by a steeper equilateral bispectrum for more luminous or higher stellar mass lenses for the excess mass. Importantly, we find the excess mass to be very sensitive to galaxy type as recently predicted with semi-analytic galaxy models: luminous ($M_r < -21$) late-type galaxies show no detectable signal, while all excess mass detected for luminous galaxies seems to be associated with early-type galaxies. We also present the first observational constraints on third-order stochastic galaxy biasing parameters.

Key words: gravitational lensing: weak – galaxies: haloes – dark matter – large-scale structure of Universe.

1 INTRODUCTION

Over the course of the last two decades, the gravitational lensing effect has allowed us to establish a new branch of science that exploits

⋆ E-mail: psimon@astro.uni-bonn.de

the distortion of light bundles from distant galaxies ('sources') in order to probe the large-scale gravitational field produced by intervening matter. Strong tidal gravitational fields cause an obvious distortion of individual galaxy images ('strong lensing'; cf. Meylan et al. 2006), whereas weak deflections can only be inferred by statistical methods utilizing many galaxy images ('weak lensing'; cf. Schneider 2006). For the latter, usually shear image distortions are harnessed, although the study of higher order flexion distortions may also be feasible in the near future (cf. Goldberg & Natarajan 2002; Goldberg & Bacon 2005; Velander, Kuijken & Schrabback 2011). Recently, the lensing magnification effect has also moved into the focus of research as a new source of information on cosmological large-scale structure (Hildebrandt, van Waerbeke & Erben 2009). As the gravitational field is solely determined by the mass density of the objects under examination, no further assumptions on their properties need to be made when studying lensing. This makes it a unique tool for cosmologists to examine the large-scale structure of the Universe, in particular the relation between luminous components, such as galaxies and the dark component. Within the current Λ cold dark matter (ΛCDM) standard model of cosmology (Peacock 1999; Dodelson 2003), the major fraction of matter is so-called dark matter, whereas ordinary baryonic matter is subdominant (Komatsu et al. 2011). Therefore, lensing plays a key role in scrutinizing the dominant matter component or in testing the standard model.

Statistical methods have been developed that quantify the average mass distribution around galaxies by cross-correlating tangential shear, as observed from background sources, with foreground lens galaxy positions. Galaxy–galaxy lensing (GGL), as the first highly successful application, in effect measures the stacked projected surface mass density profiles around galaxies (Brainerd, Blandford & Smail 1996; Hudson et al. 1998; Fischer et al. 1999; McKay et al. 2001; Hoekstra et al. 2003; Hoekstra, Yee & Gladders 2004; Seljak & Warren 2004; Sheldon et al. 2004; Kleinheinrich et al. 2006; Mandelbaum et al. 2006a; Parker et al. 2007; van Uitert et al. 2011; Leauthaud et al. 2012; Mandelbaum et al. 2012). The GGL signal is thus a function of lens–source separation (and their redshifts) only, i.e. a two-point statistic that is based on a lens and the image ellipticity of a source galaxy. For a review see Schneider (2006) or Hoekstra & Jain (2008). GGL studies revealed, e.g. a mass distribution far exceeding the extension of visible light: lenses are embedded in a dark matter halo of a size with at least $\sim 100\,h^{-1}$ kpc (Hoekstra et al. 2004) and a mean density profile consistent with those found in ΛCDM simulations (Navarro, Frenk & White 1996; Springel et al. 2005). As an extension of GGL, the light distribution within the lens can be utilized to align the stacked mass fields, which allows the measurement of the mean ellipticity of the halo mass distribution in a coordinate frame aligned with the stellar light distribution of a lens (Hoekstra et al. 2004; Mandelbaum et al. 2006b; van Uitert et al. 2012; Schrabback & CFHTLenS team 2012, in preparation). More generally, on larger spatial scales the technique has been exploited to infer the spatial distribution of lenses with respect to the matter distribution, the second-order galaxy biasing (Hoekstra, Yee & Gladders 2001; Hoekstra, Van Waerbeke & Gladders 2002; Pen et al. 2003; Sheldon et al. 2004; Seljak et al. 2005; Simon et al. 2007; Jullo et al. 2012). More recently, GGL in combination with galaxy clustering in redshift surveys has been employed to test general relativity (Reyes et al. 2010), or to successfully constrain cosmological parameters (Mandelbaum et al. 2012).

Schneider & Watts (2005, SW05 hereafter) introduced two new GGL correlation functions that involve three instead of two galaxies, either two lenses and one source ('lens–lens–shear') or two sources and one lens ('lens–shear–shear'). Therefore, this new class of correlators represents the third-order level of GGL or simply galaxy–galaxy–galaxy lensing ('G3L'). Both correlators express new aspects of the average matter distribution around lenses, which can be translated into third-order galaxy biasing parameters (SW05), especially if represented in terms of aperture statistics (Schneider 1998). This paper chooses the aperture statistics to represent the G3L signal. Thereby, we essentially express the angular bispectrum of the (projected) matter–galaxy three-point correlation. A rigorous mathematical description of the aperture statistics is given in the following section.

A more intuitive interpretation (Simon, Schneider & Kübler 2012) of G3L is given by the definition of the real-space correlation functions: the lens–lens–shear correlation function measures the average excess shear (or excess mass, Simon et al. 2008) around clustered lens pairs, i.e. in excess of the average shear pattern around pairs formed from a hypothetical set of lenses that is uniformly randomly distributed on the sky (unclustered) but exhibit the same GGL signal as the lenses in the data. It is a probe for the joint matter environment of galaxy pairs, not single galaxies. This correlator promises to put additional constraints on galaxy models (Saghiha et al. 2012) as it appears to be very sensitive to galaxy types. On the other hand, the lens–shear–shear correlation function measures the 'excess shear–shear correlation': it quantifies the shear–shear correlation function in the neighbourhood of a lens in excess of shear–shear correlations as expected from randomly scattered lenses. Thereby it picks up the (projected) matter density two-point correlation function of matter physically associated with lenses. In a way this makes the lens–shear–shear correlator similar to the traditional GGL, but now also probing the variance in the surface matter density around lenses instead of merely the average. The angular matter–galaxy bispectra are Fourier transforms of these correlators.

Simon et al. (2008) have demonstrated with the Red-Sequence Cluster Survey (RCS1; Gladders & Yee 2005) that both G3L correlation functions can readily be measured with existing lensing surveys. The RCS1 study aimed to obtain a high signal-to-noise ratio of the lensing signal, for which all available lenses were combined into one lens catalogue. Therefore, apart from this feasibility study in existing data, little more is known on the dependence of the G3L signal on galaxy properties. This paper is a first step to fill this gap by systematically measuring G3L for a series of lens samples with varying properties. The amount of data available through the Canada–France–Hawaii Telescope Lensing Survey (CFHTLenS) analysis allows this to be done for the first time. An accompanying paper by Velander et al. (2012) explores the GGL signal of CFHTLenS in the light of the halo model (Cooray & Sheth 2002).

The paper is laid out as follows. Section 2 summarizes the aperture statistics that are devised to express the G3L signal, give their practical estimators and list possible sources of systematics. In Section 3, we outline the selection criteria of our source and lens samples. Lenses are selected by luminosity, stellar mass, redshift and two galaxy spectral types, all to be analysed separately. Section 4 presents our G3L results. For a large range of angular scales covered in this study, the G3L signal is characterized by a simple power law whose parameters are given. Section 5 offers a physical interpretation of the G3L statistics in terms of 3D galaxy–matter bispectra. In this context, we also introduce a normalization scheme to remove, to the lowest order, the impact of the exact shape of the lens redshift distribution and the source redshift distribution from the signal. Finally, the Sections 6 and 7 present our discussion and conclusions.

Throughout the paper, we adopt a *Wilkinson Microwave Anisotropy Probe* 7 (*WMAP*7) (Komatsu et al. 2011) fiducial cosmology for the matter density $\Omega_\mathrm{m} = 0.27$, the cosmological constant $\Omega_\Lambda = 1 - \Omega_\mathrm{m} = 0.73$ (both in units of the critical density) and $H_0 = 100\,h\,\mathrm{km\,s^{-1}\,Mpc^{-1}}$. These parameters are consistent with gravitational lensing constraints obtained from CFHTLenS itself (Benjamin et al. 2012; Kilbinger et al. 2012; Heymans et al., submitted). If not stated otherwise, we explicitly use $h = 0.73$, in particular for the absolute galaxy magnitudes and their stellar masses.

2 FORMALISM

This section summarizes the theory and notation of G3L as detailed in SW05, and lists possible G3L specific systematics.

2.1 Galaxy–galaxy lensing preliminaries

The weak gravitational lensing effect (see Schneider 2006, and references therein) probes the three-dimensional relative matter density fluctuations $\delta_\mathrm{m}(\boldsymbol{R}_\perp, \chi) = \Delta\rho_\mathrm{m}/\bar{\rho}_\mathrm{m}$ in projection along the line of sight in terms of the lensing convergence

$$\kappa(\boldsymbol{\theta}) = \frac{3\Omega_\mathrm{m}}{2D_\mathrm{H}^2}\int_0^{\chi_\mathrm{h}} \mathrm{d}\chi\, \frac{g(\chi) f_\mathrm{K}(\chi)}{a(\chi)}\, \delta_\mathrm{m}(f_\mathrm{K}(\chi)\boldsymbol{\theta}, \chi)\,. \tag{1}$$

Here $\boldsymbol{R}_\perp = f_\mathrm{K}(\chi)\boldsymbol{\theta}$ is a 2D vector perpendicular to a reference line of sight and $\boldsymbol{\theta}$ the angular position on the sky. The comoving angular diameter distance $f_\mathrm{K}(\chi)$ is written as a function of comoving radial distance χ. By $D_\mathrm{H} := c/H_0$ we define the Hubble length, and $a(\chi)$ is the cosmic scale factor at a distance χ; we set $a(0) = 1$ by definition; c is the vacuum speed of light. By χ_h we denote the comoving Hubble radius of today as the theoretical maximum distance at which we can observe objects. The lensing efficiency averaged over the probability density distribution function (pdf) $p_\mathrm{b}(\chi)\,\mathrm{d}\chi$ of background galaxies ('sources') is expressed by

$$g(\chi) = \int_\chi^{\chi_\mathrm{h}} \mathrm{d}\chi'\, p_\mathrm{b}(\chi')\frac{f_\mathrm{K}(\chi'-\chi)}{f_\mathrm{K}(\chi')}\,. \tag{2}$$

Although the convergence in principle is observable through magnification of galaxy images, past weak lensing analyses and this paper focus on the related gravitational shear (Kaiser & Squires 1993)

$$\gamma_\mathrm{c}(\boldsymbol{\theta}) = \frac{1}{\pi}\int \mathrm{d}^2\vartheta\, \mathcal{D}(\boldsymbol{\vartheta}-\boldsymbol{\theta})\kappa(\boldsymbol{\vartheta})\,; \quad \mathcal{D}(\boldsymbol{\theta}) := -\frac{1}{(\boldsymbol{\theta}^*)^2}\,. \tag{3}$$

By $\boldsymbol{\theta}^*$ we denote the complex conjugate of $\boldsymbol{\theta}$. For this purpose, the complex ellipticity of the galaxy image

$$\epsilon(\boldsymbol{\theta}) \approx \gamma_\mathrm{c}(\boldsymbol{\theta}) + \epsilon_\mathrm{s}\,; \quad \langle\epsilon_\mathrm{s}\rangle = 0 \tag{4}$$

serves as a noisy estimator of γ_c; the noise term originates from the unknown intrinsic shape ϵ_s. In addition, due to the finite number of sources, one also experiences sampling noise of the shear field. Note that we adopt the commonly used complex notation of 2D vectors and spinors (in the case of shears and ellipticities), where real and imaginary parts are the components along two Cartesian axes in a tangential plane on the sky.

GGL techniques correlate the total matter distribution $\kappa(\boldsymbol{\theta})$ with the relative number density distribution $\kappa_\mathrm{g}(\boldsymbol{\theta})$ of lens galaxies ('lenses') on the sky by means of cross-correlating the lensing signal with positions of foreground galaxies,

$$\kappa_\mathrm{g}(\boldsymbol{\theta}) = \frac{n_\mathrm{g}(\boldsymbol{\theta}) - \bar{n}_\mathrm{g}}{\bar{n}_\mathrm{g}} = \int_0^{\chi_\mathrm{h}} \mathrm{d}\chi\; p_\mathrm{f}(\chi)\,\delta_\mathrm{g}(f_\mathrm{K}(\chi)\boldsymbol{\theta}, \chi)\,, \tag{5}$$

where $p_\mathrm{f}(\chi)\,\mathrm{d}\chi$ is the pdf of the lens (foreground) comoving distances along the line of sight; $n_\mathrm{g}(\boldsymbol{\theta})$ is the projected number density of lenses and $\bar{n}_\mathrm{g}$ its statistical mean. For the scope of this paper, $p_\mathrm{f}(\chi)$ is estimated from a redshift pdf $p_z(z)\,\mathrm{d}z = p_\mathrm{f}(\chi)\,\mathrm{d}\chi$ of a selected lens sample.

2.2 G3L aperture statistics

For practical purposes, the aperture statistics are a convenient measure for a lensing analysis (Schneider 1998; Schneider et al. 1998; van Waerbeke 1998; Crittenden et al. 2002). They quantify moments of fluctuations in $\kappa(\boldsymbol{\theta})$ and $\kappa_\mathrm{g}(\boldsymbol{\theta})$ within apertures of a variable angular scale θ. The moments are determined from the smoothed fields $\kappa(\boldsymbol{\theta})$ and $\kappa_\mathrm{g}(\boldsymbol{\theta})$,

$$M_\mathrm{ap}(\theta) = \int \frac{\mathrm{d}^2\vartheta}{\theta^2}\, u\left(|\boldsymbol{\vartheta}|\theta^{-1}\right)\, \kappa\,(\boldsymbol{\vartheta})\,, \tag{6}$$

$$\mathcal{N}(\theta) = \int \frac{\mathrm{d}^2\vartheta}{\theta^2}\, u\left(|\boldsymbol{\vartheta}|\theta^{-1}\right)\, \kappa_\mathrm{g}(\boldsymbol{\vartheta})\,, \tag{7}$$

where $u(\vartheta/\theta)\theta^{-2}$ is the smoothing kernel. For mathematical convenience, we placed the aperture centre at $\boldsymbol{\theta}_\mathrm{c} = 0$ in the previous definition. Third-order moments are defined by considering the ensemble average of

$$\langle\mathcal{N}^2 M_\mathrm{ap}\rangle(\theta_1;\theta_2;\theta_3) := \langle\mathcal{N}(\theta_1)\mathcal{N}(\theta_2)M_\mathrm{ap}(\theta_3)\rangle\,, \tag{8}$$

$$\langle\mathcal{N} M_\mathrm{ap}^2\rangle(\theta_1;\theta_2;\theta_3) := \langle\mathcal{N}(\theta_1)M_\mathrm{ap}(\theta_2)M_\mathrm{ap}(\theta_3)\rangle\,, \tag{9}$$

over all random realizations of the fields $\kappa(\boldsymbol{\theta})$ and $\kappa_\mathrm{g}(\boldsymbol{\theta})$. Due to the assumed statistical homogeneity of the fields, the averages do not depend on the aperture centre position. Therefore, in practice, where only one realization or survey is available, these quantities are estimated by averaging the products $\mathcal{N}(\theta_1)\mathcal{N}(\theta_2)M_\mathrm{ap}(\theta_3)$ and $\mathcal{N}(\theta_1)M_\mathrm{ap}(\theta_2)M_\mathrm{ap}(\theta_3)$ for different aperture centres covering the survey area. See Fig. 1 for an illustration.

For a compensated filter u, i.e. $\int_0^\infty \mathrm{d}\theta\,\theta u(\theta) = 0$, the aperture mass can in principle be obtained directly from the observable shear through (Schneider et al. 1998)

$$M_\mathrm{ap}(\theta) = \int_0^\infty \int_0^{2\pi} \frac{\mathrm{d}\varphi\,\mathrm{d}\vartheta\,\vartheta}{\theta^2}\, q(\vartheta\theta^{-1})\,\Re(\gamma(\boldsymbol{\vartheta};\varphi))\,, \tag{10}$$

where $\gamma(\boldsymbol{\vartheta};\varphi) := -\mathrm{e}^{-2\mathrm{i}\varphi}\gamma_\mathrm{c}(\boldsymbol{\vartheta})$ denotes the Cartesian shear γ_c at angular position $\boldsymbol{\vartheta}$ rotated by the polar angle φ. The real part of $\gamma(\boldsymbol{\vartheta};\varphi)$ is the tangential shear, the imaginary part the cross shear. The relation between the filters $u(x)$ and $q(x)$ is given by

$$q(x) = \left(\frac{2}{x^2}\int_0^x \mathrm{d}s\, s\, u(s)\right) - u(x)\,. \tag{11}$$

This paper uses the exponential aperture filter from van Waerbeke (1998), exponential filter hereafter,

$$u(x) = \frac{1}{2\pi}\left(1 - \frac{x^2}{2}\right)\mathrm{e}^{-x^2/2}\,, \tag{12}$$

which effectively has a finite support because of the Gaussian factor that suppresses the filter strongly to zero for $\vartheta \gtrsim 3\theta$ (SW05). The Fourier transform of the aperture filter is

$$\tilde{u}(\ell) = \int \mathrm{d}^2\theta\, u(\theta)\mathrm{e}^{+\mathrm{i}\boldsymbol{\ell}\cdot\boldsymbol{\theta}} = \frac{\ell^2}{2}\mathrm{e}^{-\ell^2/2}\,. \tag{13}$$

We generally denote a Fourier transform of $f(\boldsymbol{\theta})$ by $\tilde{f}(\boldsymbol{\ell})$ in the following. The exponential filter $\tilde{u}(\ell)$ peaks in Fourier space at an

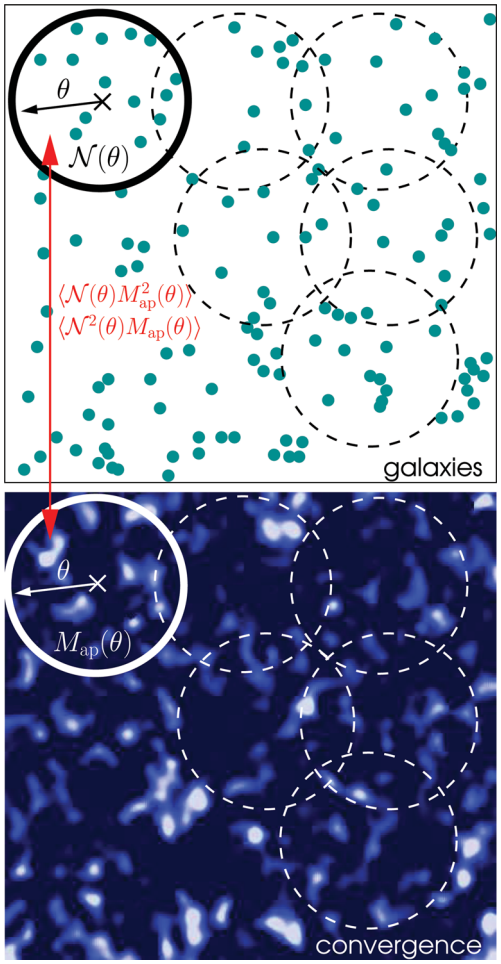

Figure 1. Illustration of the aperture statistics. Fluctuations $\mathcal{N}(\theta)$ in the projected galaxy number density (*top panel*), smoothed to the characteristic filter scale θ, are statistically compared to the filtered projected matter fluctuations $M_{\rm ap}(\theta)$ (lensing convergence; *bottom panel*). We take $\mathcal{N}^2(\theta)M_{\rm ap}(\theta)$ or $\mathcal{N}(\theta)M_{\rm ap}^2(\theta)$, and average these for different aperture centres (dashed circles) to estimate third-order moments of the joint probability distribution of $\mathcal{N}(\theta)$ and $M_{\rm ap}(\theta)$.

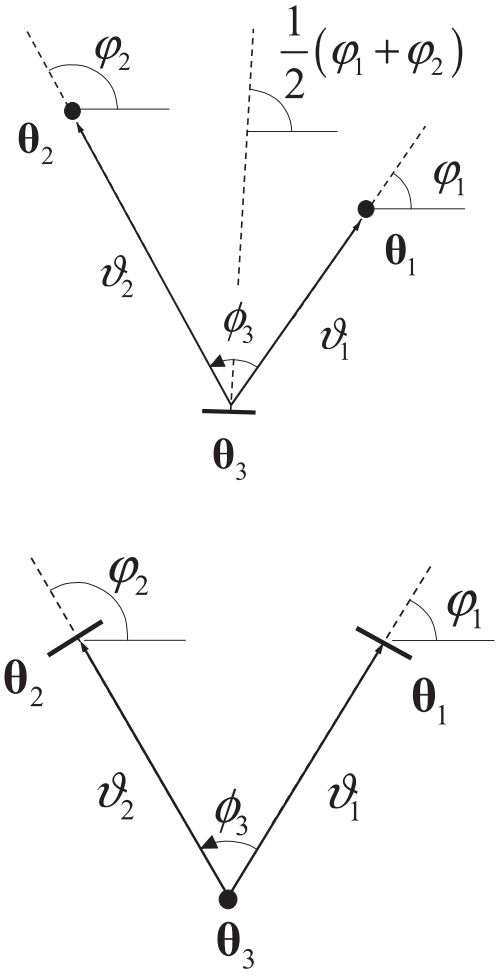

Figure 2. Illustration of the parametrization of the lens–lens–shear three-point correlator $\widetilde{\mathcal{G}}(\vartheta_1, \vartheta_2, \phi_3)$ (*top panel*), and the lens–shear–shear correlation function $\widetilde{G}_{\pm}(\vartheta_1, \vartheta_2, \phi_3)$ (*bottom panel*). These statistics are employed to estimate the aperture statistics in Fig. 1. The figure is copied from SW05.

angular wavenumber of $\ell = \sqrt{2}$, which determines a characteristic angular scale selected by an aperture radius of θ.

2.3 Aperture statistics estimators

To obtain the third-order moments of the galaxy–matter aperture statistics, we utilize the lens–lens–shear correlation function $\mathcal{G}$ in the case of $\langle\mathcal{N}^2 M_{\rm ap}\rangle$ and the lens–shear–shear correlation function $G_{\pm}$ for $\langle\mathcal{N}M_{\rm ap}^2\rangle$. This section provides only a brief description of this approach. For more details, its computationally optimized implementation as well as verification, we refer the reader to section 3 of Simon et al. (2008).

In practice, the aperture moments $\langle\mathcal{N}^2 M_{\rm ap}\rangle$ or $\langle\mathcal{N}M_{\rm ap}^2\rangle$ are not computed from the aperture mass $M_{\rm ap}$ or aperture number counts $\mathcal{N}$ directly. The information contained in the aperture statistics is also contained inside two classes of three-point correlation functions (SW05), which are relatively straightforward to estimate. Once the correlation functions have been determined, they can be transformed to the corresponding aperture statistics by an integral transformation. The estimation process thus proceeds in two basic steps. In the first step, for $\langle\mathcal{N}^2 M_{\rm ap}\rangle$ one estimates the source tangential ellipticity relative to the midpoint connecting two lenses,

$$\widetilde{\mathcal{G}}(\vartheta_1, \vartheta_2, \phi_3) = \frac{1}{\bar{n}_{\rm g}^2}\left\langle n_{\rm g}(\boldsymbol{\theta}_1) n_{\rm g}(\boldsymbol{\theta}_2)\gamma\left(\boldsymbol{\theta}_3; \frac{\varphi_1+\varphi_2}{2}\right)\right\rangle . \quad (14)$$

The meaning of the notation is illustrated in the left-hand panel of Fig. 2. For $\langle\mathcal{N}M_{\rm ap}^2\rangle$ one estimates the correlation of the ellipticities of two sources relative to the line connecting the sources as a function of separation from one lens (right-hand panel),

$$\widetilde{G}_{\pm}(\vartheta_1, \vartheta_2, \phi_3) = \frac{1}{\bar{n}_{\rm g}}\left\langle \gamma(\boldsymbol{\theta}_1; \varphi_1)\gamma^{\pm}(\boldsymbol{\theta}_2; \varphi_2) n_{\rm g}(\boldsymbol{\theta}_3)\right\rangle . \quad (15)$$

Here and in the following equations a superscript '±' as in $\gamma^{\pm}$ means γ for γ^- (in case of $\widetilde{G}_-$) and the complex conjugate γ^* for γ^+ (in case of $\widetilde{G}_+$).

Both correlation functions are estimated inside the *bins of similar triangles*, i.e. lens–source triples within a configuration of comparable side lengths $\vartheta_{1,2}$ and opening angles ϕ_3, by summing over all relevant galaxy triplets. Any triple of three galaxy positions $\boldsymbol{\theta}_i, \boldsymbol{\theta}_j, \boldsymbol{\theta}_k$ that meets the criteria of a relevant triangle is flagged by $\Delta_{ijk}^{\vartheta_1\vartheta_2\phi_3} = 1$ and $\Delta_{ijk}^{\vartheta_1\vartheta_2\phi_3} = 0$ otherwise. For this study, we utilize 100 logarithmic bins for both ϑ_1 and ϑ_2, and 100 linear bins for the

opening angle ϕ_3. For estimating $\widetilde{\mathcal{G}}$ we utilize

$$\widetilde{\mathcal{G}}^{\rm est}(\vartheta_1,\vartheta_2,\phi_3) = \frac{-\sum_{i=1}^{N_{\rm d}}\sum_{j=1}^{N_{\rm d}}\sum_{k=1}^{N_{\rm s}} w_k\,\epsilon_k\,{\rm e}^{-{\rm i}(\varphi_i+\varphi_j)}[1+\omega(|\boldsymbol{\theta}_i-\boldsymbol{\theta}_j|)]\Delta_{ijk}^{\vartheta_1\vartheta_2\phi_3}}{\sum_{i=1}^{N_{\rm d}}\sum_{j=1}^{N_{\rm d}}\sum_{k=1}^{N_{\rm s}} w_k\,\Delta_{ijk}^{\vartheta_1\vartheta_2\phi_3}}\,, \tag{16}$$

and for $\widetilde{G}_\pm$ the estimator

$$\widetilde{G}_\pm^{\rm est}(\vartheta_1,\vartheta_2,\phi_3) = \frac{\sum_{i=1}^{N_{\rm d}}\sum_{j=1}^{N_{\rm s}}\sum_{k=1}^{N_{\rm s}} w_j\,w_k\,\epsilon_j\epsilon_k^{\pm}{\rm e}^{-2{\rm i}\varphi_j}{\rm e}^{\pm 2{\rm i}\varphi_k}\,\Delta_{ijk}^{\vartheta_1\vartheta_2\phi_3}}{\sum_{i=1}^{N_{\rm d}}\sum_{j=1}^{N_{\rm s}}\sum_{k=1}^{N_{\rm s}} w_j\,w_k\,\Delta_{ijk}^{\vartheta_1\vartheta_2\phi_3}}\,, \tag{17}$$

where $N_{\rm d}$ and $N_{\rm s}$ are the number of lenses and sources, w_i are statistical weights of sources, φ_i are polar angles of the position vectors of galaxies with respect to the coordinate origin, ϵ_i are the source ellipticities, and

$$\omega(|\boldsymbol{\Delta\theta}|) = \langle\kappa_{\rm g}(\boldsymbol{\theta})\kappa_{\rm g}(\boldsymbol{\theta}+\boldsymbol{\Delta\theta})\rangle \tag{18}$$

is the angular two-point clustering of the lenses (e.g. Peebles 1980). In this paper, the angular clustering of lenses is estimated by means of the estimator in Landy & Szalay (1993) prior to the estimation of $\widetilde{\mathcal{G}}$ and then interpolated. Sources are weighed by the inverse-variance uncertainty in the *lensfit* ellipticity measurement (Miller et al. 2012).

In the second step, we transform the estimates of $\widetilde{\mathcal{G}}$ and $\widetilde{G}_\pm$ to the aperture statistics by devising the transformation integrals equations 57, 59 and 63 in SW05. There is no need to remove the unconnected terms in the correlation functions. As shown in SW05 (section 7.2 therein), the transformation from $\mathcal{G}$ to $\langle\mathcal{N}^2M_{\rm ap}\rangle$ yields the same result when $\widetilde{\mathcal{G}}$ is taken instead of $\mathcal{G}$. Therefore, the integral transformation automatically ignores unconnected second-order terms in the triple correlator, resulting in aperture statistics that are only determined by pure (connected) third-order correlation terms. The same holds true for $\widetilde{G}_\pm$ and $\langle\mathcal{N}M_{\rm ap}^2\rangle$.

2.4 Relation to 3D galaxy–matter bispectra

The aperture statistics are directly connected to the angular cross-bispectra of the projected matter and lens distribution

$$\langle\mathcal{N}^2M_{\rm ap}\rangle(\theta_1;\theta_2;\theta_3) = \int\frac{{\rm d}^2\ell_1}{(2\pi)^2}\int\frac{{\rm d}^2\ell_2}{(2\pi)^2}\tilde{u}(\ell_1\theta_1)\tilde{u}(\ell_2\theta_2)\tilde{u}(|\boldsymbol{\ell_1}+\boldsymbol{\ell_2}|\theta_3)b_{\rm gg\kappa}(\boldsymbol{\ell_1},\boldsymbol{\ell_2})\,, \tag{19}$$

$$\langle\mathcal{N}M_{\rm ap}^2\rangle(\theta_1;\theta_2;\theta_3) = \int\frac{{\rm d}^2\ell_1}{(2\pi)^2}\int\frac{{\rm d}^2\ell_2}{(2\pi)^2}\tilde{u}(\ell_1\theta_1)\tilde{u}(\ell_2\theta_2)\tilde{u}(|\boldsymbol{\ell_1}+\boldsymbol{\ell_2}|\theta_3)b_{\kappa\kappa\rm g}(\boldsymbol{\ell_1},\boldsymbol{\ell_2})\,, \tag{20}$$

where the angular galaxy–galaxy–matter bispectrum is

$$\langle\tilde{\kappa}_{\rm g}(\boldsymbol{\ell}_1)\tilde{\kappa}_{\rm g}(\boldsymbol{\ell}_2)\tilde{\kappa}(\boldsymbol{\ell}_3)\rangle = (2\pi)^2\delta_{\rm D}^{(2)}(\boldsymbol{\ell}_1+\boldsymbol{\ell}_2+\boldsymbol{\ell}_3)b_{\rm gg\kappa}(\boldsymbol{\ell_1},\boldsymbol{\ell_2}) \tag{21}$$

and the angular matter–matter–galaxy bispectrum is

$$\langle\tilde{\kappa}(\boldsymbol{\ell}_1)\tilde{\kappa}(\boldsymbol{\ell}_2)\tilde{\kappa}_{\rm g}(\boldsymbol{\ell}_3)\rangle = (2\pi)^2\delta_{\rm D}^{(2)}(\boldsymbol{\ell}_1+\boldsymbol{\ell}_2+\boldsymbol{\ell}_3)b_{\kappa\kappa\rm g}(\boldsymbol{\ell_1},\boldsymbol{\ell_2})\,. \tag{22}$$

For statistically homogeneous random fields, the triple correlators on the left-hand side of the previous two equations can only be non-vanishing when $\boldsymbol{\ell}_1+\boldsymbol{\ell}_2+\boldsymbol{\ell}_3=\boldsymbol{0}$, which is reflected by the 2D Dirac delta functions $\delta_{\rm D}^{(2)}(\boldsymbol{x})$ on the right-hand sides. Owing to homogeneity, the bispectra thus depend only on two independent arguments $\boldsymbol{\ell}$, for which we arbitrarily choose $\boldsymbol{\ell}_1$ and $\boldsymbol{\ell}_2$. This automatically implies $\boldsymbol{\ell}_3=-(\boldsymbol{\ell}_1+\boldsymbol{\ell}_2)$. In addition, the statistical isotropy implies that the bispectra are solely functions of the moduli of $\boldsymbol{\ell}_{1,2}$ and the angle enclosed by both wave vectors.

As can be seen from equations (19) and (20), the aperture statistics are a locally filtered version of the bispectrum because the exponential u-filter is relatively localized in ℓ-space with a filter maximum at $\ell_{\rm max}=\sqrt{2}/\theta$. By means of filtering, the aperture statistics basically become a band power bispectrum version of $b_{\rm gg\kappa}$ or $b_{\kappa\kappa\rm g}$. Hence the aperture statistics equations (8) and (9) measure two different angular galaxy–matter band power cross-bispectra.

By virtue of the Limber approximation (Kaiser 1992; Bartelmann & Schneider 2001) the angular bispectra and thereby the aperture statistics equations (19) and (20) can directly be related to the 3D cross-bispectrum of the matter and lens distribution (SW05) as primary physical quantities that are assessed by the statistics

$$b_{\rm gg\kappa}(\boldsymbol{\ell}_1,\boldsymbol{\ell}_2) = \frac{3\Omega_{\rm m}}{2D_{\rm H}^2}\int_0^{\chi_{\rm h}}{\rm d}\chi\,\frac{g(\chi)p_{\rm f}^2(\chi)}{f_{\rm K}^3(\chi)a(\chi)}B_{\rm ggm}\left(\frac{\boldsymbol{\ell}_1}{f_{\rm K}(\chi)},\frac{\boldsymbol{\ell}_2}{f_{\rm K}(\chi)},\chi\right)\,, \tag{23}$$

$$b_{\kappa\kappa\rm g}(\boldsymbol{\ell}_1,\boldsymbol{\ell}_2) = \frac{9\Omega_{\rm m}^2}{4D_{\rm H}^4}\int_0^{\chi_{\rm h}}{\rm d}\chi\,\frac{g^2(\chi)p_{\rm f}(\chi)}{f_{\rm K}^2(\chi)a^2(\chi)}B_{\rm mmg}\left(\frac{\boldsymbol{\ell}_1}{f_{\rm K}(\chi)},\frac{\boldsymbol{\ell}_2}{f_{\rm K}(\chi)},\chi\right)\,, \tag{24}$$

where the 3D bispectra are determined by the Fourier transforms of the matter density contrast, $\tilde{\delta}_{\rm m}(\boldsymbol{k},\chi)$, and galaxy number density contrast, $\tilde{\delta}_{\rm g}(\boldsymbol{k},\chi)$, at radial distance χ, namely

$$\langle\tilde{\delta}_{\rm g}(\boldsymbol{k}_1,\chi)\tilde{\delta}_{\rm g}(\boldsymbol{k}_2,\chi)\tilde{\delta}_{\rm m}(\boldsymbol{k}_3,\chi)\rangle = (2\pi)^3\delta_{\rm D}^{(3)}(\boldsymbol{k}_1+\boldsymbol{k}_2+\boldsymbol{k}_3)B_{\rm ggm}(\boldsymbol{k}_1,\boldsymbol{k}_2,\chi)\,, \tag{25}$$

$$\langle\tilde{\delta}_{\rm m}(\boldsymbol{k}_1,\chi)\tilde{\delta}_{\rm m}(\boldsymbol{k}_2,\chi)\tilde{\delta}_{\rm g}(\boldsymbol{k}_3,\chi)\rangle = (2\pi)^3\delta_{\rm D}^{(3)}(\boldsymbol{k}_1+\boldsymbol{k}_2+\boldsymbol{k}_3)B_{\rm mmg}(\boldsymbol{k}_1,\boldsymbol{k}_2,\chi)\,. \tag{26}$$

The vector $\boldsymbol{k}$ is the comoving wavenumber of modes entering the triple correlator. As before with the angular bispectra, the spatial bispectra are also isotropic, i.e. they are only functions of $|\boldsymbol{k}_1|$, $|\boldsymbol{k}_2|$ and the angle spanned by $\boldsymbol{k}_1$ and $\boldsymbol{k}_2$.

To refine the previous RCS1 measurement in Simon et al. (2008) for different galaxy populations, we focus on equally sized apertures with $\theta_1=\theta_2=\theta_3$ only. This leads us to the short hand notations $\langle\mathcal{N}^2M_{\rm ap}\rangle(\theta):=\langle\mathcal{N}^2M_{\rm ap}\rangle(\theta;\theta;\theta)$, likewise for $\langle\mathcal{N}M_{\rm ap}^2\rangle$. Due to the action of the u-filter in the equations (19) and (20) this picks up mainly bispectrum contributions from equilateral triangles $|\boldsymbol{\ell}_1|=|\boldsymbol{\ell}_2|=|\boldsymbol{\ell}_1+\boldsymbol{\ell}_2|$, albeit also mixing in signal from other triangles because of the finite width of the u-filter in ℓ-space.

2.5 Systematics indicators

The gravitational shear of distant galaxy images is produced by small fluctuations $\delta\phi$ in the intervening gravitational potential. To

the lowest order in $\delta\phi/c^2$ this is expected to only produce curl-free shear fields (B-modes vanish). Current surveys do not have the power to measure higher order effects, such that we expect these to be undetectable in our data. Shear-related correlation functions, or aperture moments involving the aperture mass, hence vanish after the rotation of all sources by 45°, i.e. after $\gamma_{\rm c}(\boldsymbol{\theta}) \mapsto -{\rm i}\,\gamma_{\rm c}(\boldsymbol{\theta})$. Translated into data analysis, a 45° rotation of the source ellipticities should result in a measurement that is statistically consistent with the experimental noise (e.g. Hetterscheidt et al. 2007). We use this as a necessary (but not sufficient) indicator for the absence of systematics in the data.

The estimator $\widetilde{G}_\pm^{\rm est}$ in equation (17) incorporates two sources with two uniquely different possibilities to probe systematics: rotating the ellipticities ϵ_j and ϵ_k of both sources results in the so-called B-mode channel of $\langle\mathcal{N}M_{\rm ap}^2\rangle(\theta)$, denoted here by $\langle\mathcal{N}M_\perp^2\rangle(\theta)$, and the P-mode channel, $\langle\mathcal{N}M_\perp M_{\rm ap}\rangle(\theta)$, if only either ϵ_j or ϵ_k are rotated. As pointed out by Schneider (2003), a P-mode is a signature of a parity-invariance violation in the shear data, which in a parity-invariant universe can only be generated by systematics in the point spread function (PSF) correction pipeline, or in the algorithm for the statistical analysis of the data. Non-vanishing B-modes, on the other hand, can have a physical cause. For example, they can be associated with the intrinsic clustering of sources (Schneider, van Waerbeke & Mellier 2002), intrinsic alignment correlations of physically close sources or intrinsic shape–shear correlations (Heymans et al. 2006, and references therein). Especially the latter two are a concern for this analysis, as these effects are known to affect the E-mode channel of the aperture statistics, which is the prime focus of this work. However, currently it is unclear by how much this really affects G3L. We discuss in the following Section 2.6 that the influence of these systematics can be suppressed by separating lenses and sources in redshift, which is carried out in our analysis.

Since the estimator $\widetilde{\mathcal{G}}^{\rm est}$ in equation (16) involves one source, there is only a single systematics indicator of $\langle\mathcal{N}^2M_{\rm ap}\rangle(\theta)$, which is a parity violation indicator, a P-mode channel. In the following, we will denote these statistics as $\langle\mathcal{N}^2M_\perp\rangle(\theta)$. As shown in SW05, the B- and P-modes of the statistics can be computed from $\widetilde{\mathcal{G}}$ and $\widetilde{G}_\pm$ directly by utilizing an alternative integral kernel in the transformation from correlation functions to aperture statistics; see their sections 7.1 and 7.2.

2.6 Reduction of intrinsic–intrinsic and shear-intrinsic correlations

One possible source of systematics is correlations with intrinsic ellipticities $\epsilon_{\rm s}$ of sources. A correlation between $\epsilon_{\rm s}$ of different sources (II-correlations) or between $\epsilon_{\rm s}$ and a fluctuation in the mass density field generating shear (GI-correlations) is known to contribute to the shear correlation functions (e.g Hirata & Seljak 2004; Heymans et al. 2006; Joachimi et al. 2011). For a discussion of intrinsic alignments in CFHTLenS see also Heymans et al. (submitted). We argue here that selecting lenses and sources from well-separated distances ideally removes contaminations by II- or GI-correlations in the G3L statistics.

Consider the galaxy number density contrasts $\kappa_{{\rm g},1}$ and $\kappa_{{\rm g},2}$ in two arbitrary line of sight directions $\boldsymbol{\theta}_1$ and $\boldsymbol{\theta}_2$, respectively, and a source ellipticity $\epsilon_{\rm s} + \gamma$ in a third direction $\boldsymbol{\theta}_3$. The shear γ and $\epsilon_{\rm s}$ are rotated in direction of the mid-point between the two lenses according to the definition of $\mathcal{G}$. If lenses and sources are well separated in distance, then their properties are statistically independent. The lens–lens–shear correlator measures

$$\begin{aligned}\mathcal{G} &= \langle\kappa_{{\rm g},1}\kappa_{{\rm g},2}(\gamma+\epsilon_{\rm s})\rangle\\ &= \langle\kappa_{{\rm g},1}\kappa_{{\rm g},2}\gamma\rangle + \langle\kappa_{{\rm g},1}\kappa_{{\rm g},2}\rangle\langle\epsilon_{\rm s}\rangle\\ &= \langle\kappa_{{\rm g},1}\kappa_{{\rm g},2}\gamma\rangle\ ,\end{aligned} \tag{27}$$

free of any systematic contribution from the intrinsic shape $\epsilon_{\rm s}$, if $\epsilon_{\rm s}$ is statistically independent of the lens number density fluctuation $\kappa_{\rm g}$, i.e.

$$\langle\kappa_{{\rm g},1}\kappa_{{\rm g},2}\epsilon_{\rm s}\rangle = \langle\kappa_{{\rm g},1}\kappa_{{\rm g},2}\rangle\langle\epsilon_{\rm s}\rangle\ , \tag{28}$$

vanishing due to $\langle\epsilon_{\rm s}\rangle = 0$.

Now, consider a lens number density contrast $\kappa_{\rm g}$ in one direction and the ellipticities $\epsilon_{{\rm s},i} + \gamma_i$ of two source images $i = 1, 2$ in two other directions. The ellipticities are rotated in direction of line connecting the sources in accordance with the definition of $G_\pm$. The triple correlator measures

$$\begin{aligned}G_\pm &= \langle\kappa_{\rm g}(\gamma_1^\pm + \epsilon_{{\rm s},1}^\pm)(\gamma_2+\epsilon_{{\rm s},2})\rangle\\ &= \langle\kappa_{\rm g}\gamma_1^\pm\gamma_2\rangle + \langle\kappa_{\rm g}\epsilon_{{\rm s},1}^\pm\gamma_2\rangle + \langle\kappa_{\rm g}\gamma_1^\pm\epsilon_{{\rm s},2}\rangle + \langle\kappa_{\rm g}\epsilon_{{\rm s},1}^\pm\epsilon_{{\rm s},2}\rangle\\ &= \langle\kappa_{\rm g}\gamma_1^\pm\gamma_2\rangle + \langle\kappa_{\rm g}\epsilon_{{\rm s},1}^\pm\gamma_2\rangle + \langle\kappa_{\rm g}\gamma_1^\pm\epsilon_{{\rm s},2}\rangle + \langle\kappa_{\rm g}\rangle\langle\epsilon_{{\rm s},1}^\pm\epsilon_{{\rm s},2}\rangle\\ &= \langle\kappa_{\rm g}\gamma_1^\pm\gamma_2\rangle + \langle\kappa_{\rm g}\epsilon_{{\rm s},1}^\pm\gamma_2\rangle + \langle\kappa_{\rm g}\gamma_1^\pm\epsilon_{{\rm s},2}\rangle\ .\end{aligned} \tag{29}$$

The last term in the third line vanishes because $\kappa_{\rm g}$ in the foreground is independent of the intrinsic shape of the sources in the background and because of $\langle\kappa_{\rm g}\rangle = 0$. The latter follows from the definition of density fluctuations $\kappa_{\rm g}$.

The last two terms in the last line are less clear. For example in $\langle\kappa_{\rm g}\epsilon_{{\rm s},1}^\pm\gamma_2\rangle$, γ_2 could be correlated with both $\epsilon_{{\rm s},1}$ (GI signal, if source 2 is behind source 1) *and* $\kappa_{\rm g}$ (GGL signal). However, on the level of accuracy of the Born approximation that is used in equation (1), the shear γ_2 is linear in the matter density contrast $\delta_{\rm m}$ up to the distance of source 2. We can, therefore, split the contributions to γ_2 into three parts $\gamma_2 = \gamma_\kappa + \gamma_\epsilon + \gamma_{\rm rest}$, namely (i) in contributions from matter within correlation length to the lens, γ_κ, (ii) matter within correlation distance to source 1, γ_ϵ and (iii) the rest $\gamma_{\rm rest}$, which is neither correlated with $\kappa_{\rm g}$ nor with $\epsilon_{{\rm s},1}$. In this case, we find

$$\langle\kappa_{\rm g}\epsilon_{{\rm s},1}^\pm\gamma_2\rangle = \langle\kappa_{\rm g}\gamma_\kappa\rangle\langle\epsilon_{{\rm s},1}^\pm\rangle + \langle\kappa_{\rm g}\rangle\langle\epsilon_{{\rm s},1}^\pm\gamma_\epsilon\rangle + \langle\kappa_{\rm g}\rangle\langle\epsilon_{{\rm s},1}^\pm\rangle\langle\gamma_{\rm rest}\rangle\ . \tag{30}$$

All three terms vanish owing to $\langle\kappa_{\rm g}\rangle = \langle\epsilon_{{\rm s},1}^\pm\rangle = 0$. A similar rational shows that also $\langle\kappa_{\rm g}\gamma_1^\pm\epsilon_{{\rm s},2}\rangle$ vanishes to the lowest order, such that we expect to find in the weak lensing regime

$$G_\pm = \langle\kappa_{\rm g}\gamma_1^\pm\gamma_2\rangle\ . \tag{31}$$

2.7 Magnification of lenses

Another conceivable systematic effect is through cosmic magnification (Narayan 1989; Bartelmann & Schneider 2001) that is generated by matter density fluctuations in front of lenses. To the lowest order, foreground matter density fluctuations with lensing convergence $\kappa_<$ (equation 1) integrated to the *lens distance* modify the observed clustering of lenses on the sky above a certain flux limit $f_{\rm lim}$ according to

$$\kappa_{\rm g}' = \kappa_{\rm g} + \lambda\kappa_< + \mathcal{O}(\kappa_<^2)\ , \tag{32}$$

compared to the unmagnified lens number density $\kappa_{\rm g}$. Here, we have $\lambda := 2(\nu - 1)$ with $\bar{n}_{\rm g}(> f_{\rm lim}) \propto f_{\rm lim}^{-\nu}$ being the mean number density of lenses with flux greater than $f_{\rm lim}$. Normally $\nu - 1$ is of the order of unity (van Waerbeke 2010) or smaller.

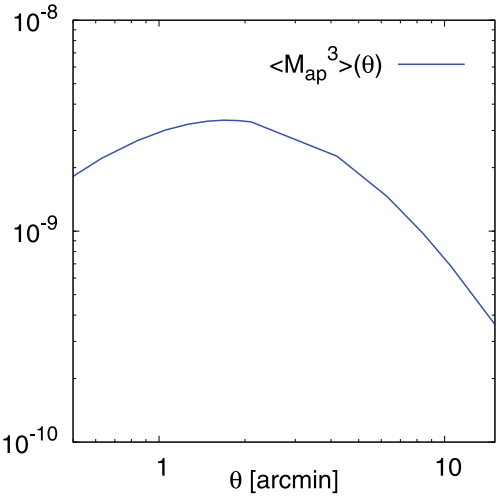

Figure 3. Prediction of the third-order moment of the aperture mass $\langle M_{\rm ap}^3 \rangle$ for sources at redshift $z_{\rm s} = 0.4$.

Likewise the shear distortion $\gamma = \gamma_< + \gamma_>$, equation (3), into the same los direction contains a contribution $\gamma_<$ related to $\kappa_<$ and $\gamma_>$ that is the shear originating from matter fluctuations beyond the foreground. This in combination produces as additional contribution to $\mathcal{G} = \langle \kappa'_{\rm g,1} \kappa'_{\rm g,2} (\gamma_< + \gamma_>) \rangle$ the term $\lambda^2 \langle \kappa_{<,1} \kappa_{<,2} \gamma_< \rangle$ and to $G_\pm = \langle \kappa'_{\rm g} (\gamma_{<,1} + \gamma_{>,1})(\gamma_{<,2} + \gamma_{>,2}) \rangle$ the term $\lambda \langle \kappa_< \gamma_{<,1} \gamma_{<,2} \rangle$.

These terms are basically third-order cosmic shear correlations or, in terms of the aperture statistics, related to the $\langle M_{\rm ap}^3(\theta) \rangle$ statistics (Schneider, Kilbinger & Lombardi 2005). Third-order shear correlations have been measured (Bernardeau, van Waerbeke & Mellier 2003; Pen et al. 2003; Jarvis, Bernstein & Jain 2004; Semboloni et al. 2011) and $\langle M_{\rm ap}^3(\theta) \rangle$ has been found (Jarvis et al. 2004; Semboloni et al. 2011) to be of the order of $\lesssim 10^{-7}$ for aperture scales of $\theta \sim 1$ arcmin and sources at $z_{\rm s} \sim 1.0$. As this includes contributions from the entire integrated matter up to $z_{\rm s}$, whereas the G3L magnification effect only contributions from the matter integrated up to the lens redshifts $z_{\rm d} \sim 0.4$, we consider this as an empirical upper limit for the magnification effect. In Fig. 3, we show a prediction of $\langle M_{\rm ap}^3(\theta) \rangle$ with sources at $z_{\rm s} = 0.4$ for a WMAP7-like cosmology based on the theory described in Semboloni et al. (2011). This result implies that the impact of lens magnification on the G3L aperture statistics is smaller than $\lesssim 10^{-8}$.

3 DATA

3.1 Object selection and photometric redshifts

This work uses the full CFHTLenS data set, which originates from the CFHTLS-Wide Survey. The CFHTLS-Wide imaged 171 MegaCam (mounted on the CFHT) pointings in the five broad-band filters u^*, g', r', i' and z'. During the observation campaign of CFHTLS, the i'-band filter was replaced by a new filter with a slightly different transmission curve. For some of the pointings only the updated i'-band filter magnitudes are available, which are treated as the old filter magnitudes in the analysis. For details, see Erben et al. (2012).

CFHTLenS has an effective area (different pointings partly overlap) of about 154 square degrees with high-quality photometric redshifts down to $i' \approx 24.7$. The data set and the extraction of our photometric redshift catalogue are described in Hildebrandt et al. (2012). Our data processing techniques and recipes are described

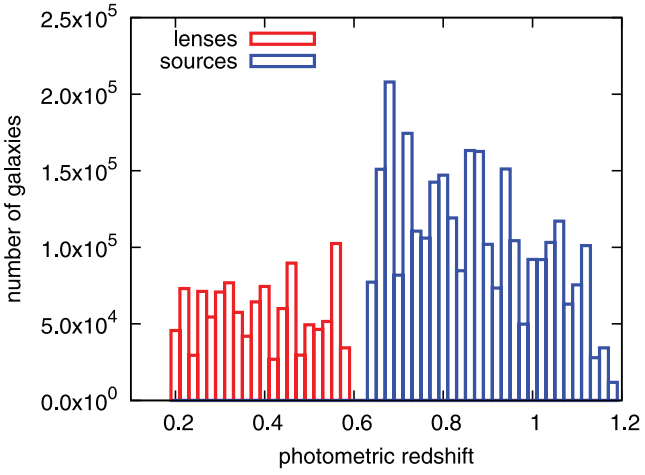

Figure 4. Total number of lenses (red) and sources (blue) in the catalogue between $0.2 \leq z_{\rm photo} < 1.2$ and $17.5 \leq i' < 22.5$ for lenses or $17.5 \leq i' < 24.7$ for sources. The figures comprise all galaxies, complying with the selection cuts, contained within all 172 pointings. For the G3L analysis, the lens sample is further subdivided in luminosity, stellar mass bins and photometric redshift, while sources are rejected for a photo-z of $z_{\rm photo} < 0.65$.

in Erben et al. (2009) and Erben et al. (2012). As primary selection criterion, we select sources brighter than $i' < 24.7$ and lenses brighter than $i' < 22.5$. This will be further subdivided in the following by using photometric redshifts (Fig. 4) and, in the case of lenses, M_r rest-frame magnitudes, stellar masses or SED information (details below). 43 pointings out of 171 exhibit a significant PSF residual signal, according to the detailed tests in section 4.2 of Heymans et al. (2012) and are therefore discarded for the analysis (∼25 per cent area); 129 pointings are included in the analysis. This leaves a total effective survey area of ∼120 deg^2 that is eventually used in the analysis. Of this area, an additional ∼20 per cent is lost due to masking. The analysis is performed on individual fields which allows us to use field-to-field variances of the measurements to estimate the covariance of measurement errors directly from the data.

3.2 Lens samples

To guarantee a high reliability of the photo-z estimates for the lenses, a magnitude cut of $i' \leq 22.5$ is applied. A detailed account and tests of the CFHTLenS photo-z pipeline can be found in Hildebrandt et al. (2012). Based on the galaxies endowed with photometric redshifts, three classes of lens samples are selected (Table 1).

(i) A luminosity or L-sample class, which consists of six distinct rest-frame M_r-bins (SDSS r-filter; York et al. 2000), labelled L1–L6. The same formal luminosity bin limits as in Mandelbaum et al. (2006a) or Velander et al. (2012) are applied, although we do not automatically expect equivalent completeness of the samples. To quantify the completeness, we introduce the $f_{\rm c}$ parameter below.

(ii) A stellar mass or sm-sample class, which is also further subdivided using seven distinct stellar mass bins. Again, we are guided by Mandelbaum et al. (2006a) for compiling this sample class. The sm class has sub-classes with labels sm1–sm7.

(iii) A galaxy type class using the `T_B` parameter in `BPZ` (Benitez 2000), which provides the most likely galaxy SED for a given galaxy and its estimated photo-z; see Erben et al. (2012) for more details. `T_B`=2 as division line, we separate early-type galaxies ('ETG'),

Table 1. Selection criteria of lens samples and source sample for the G3L analysis applied to the samples in Fig. 4, following Mandelbaum et al. (2006a) for the lenses. The luminosity bins (L), stellar mass bins (sm) and galaxy type bins (ETG: early-type galaxies; LTG: late-type galaxies) are again subdivided by $0.2 \leq z_{\rm photo} < 0.44$ ('low-z') and $0.44 \leq z_{\rm photo} < 0.6$ ('high-z'). Sources attributed no statistical weight w by *lensfit* are not used in the source sample. The galaxy numbers are for all pointings of which the final analysis discards roughly 25 per cent. Luminosities and stellar masses assume $h = 0.73$. (1) $\bar{z}$: mean redshift, σ_z: rms variance of $p(z)$; (2) and (3): best-fitting parameters of $\omega(\theta) = A_\omega(\theta/1')^{-\lambda} + {\rm IC}$ within $0'.2 \leq \theta < 10'$; (4): sample completeness; (5): mean r-band luminosity; (6): mean stellar mass in units of 10^{10} $M_\odot$.

Sample	Selection	No. of Galaxies	$\bar{z} \pm \sigma_z^{(1)}$	$A_\omega/0.1^{(2)}$	$\lambda^{(3)}$	$f_c^{(4)}$	$\langle M_r\rangle^{(5)}$	$\langle M_*\rangle^{(6)}$
L1 low-z	$-18 \leq M_r < -17$	36 372	0.22 ± 0.16	2.40 ± 0.29	0.45 ± 0.11	0.14	-17.75	0.04
L1 high-z	"	–	–	–	–	–	–	–
L2 low-z	$-19 \leq M_r < -18$	157 306	0.28 ± 0.15	1.91 ± 0.23	0.35 ± 0.05	0.45	-18.60	0.10
L2 high-z	"	–	–	–	–	–	–	–
L3 low-z	$-20 \leq M_r < -19$	220 329	0.34 ± 0.14	1.41 ± 0.12	0.43 ± 0.05	0.81	-19.52	0.26
L3 high-z	"	75 902	0.48 ± 0.11	1.63 ± 0.18	0.54 ± 0.08	0.42	-19.72	0.29
L4 low-z	$-21 \leq M_r < -20$	149 190	0.34 ± 0.12	1.63 ± 0.07	0.53 ± 0.03	0.95	-20.50	0.91
L4 high-z	"	185 286	0.51 ± 0.10	1.62 ± 0.08	0.69 ± 0.04	0.82	-20.53	0.98
L5 low-z	$-22 \leq M_r < -21$	88 916	0.34 ± 0.11	2.19 ± 0.14	0.60 ± 0.05	0.98	-21.48	3.09
L5 high-z	"	134 369	0.51 ± 0.09	2.06 ± 0.05	0.74 ± 0.02	0.99	-21.49	3.06
L6 low-z	$-23 \leq M_r < -22$	31 373	0.35 ± 0.10	3.02 ± 0.24	0.65 ± 0.07	0.99	-22.40	8.56
L6 high-z	"	55 315	0.52 ± 0.08	2.50 ± 0.10	0.92 ± 0.04	1.00	-22.42	8.11
sm1 low-z	$0.5 \leq M_*/10^{10}\,{\rm M}_\odot < 1.0$	78 181	0.34 ± 0.12	2.41 ± 0.34	0.43 ± 0.09	0.94	-20.49	0.71
sm1 high-z	"	69 784	0.50 ± 0.10	1.72 ± 0.33	0.58 ± 0.15	0.77	-20.66	0.73
sm2 low-z	$1.0 \leq M_*/10^{10}\,{\rm M}_\odot < 2.0$	61 650	0.34 ± 0.11	3.75 ± 0.82	0.36 ± 0.11	0.98	-20.98	1.42
sm2 high-z	"	82 411	0.51 ± 0.09	2.39 ± 0.07	0.60 ± 0.07	0.90	-20.99	1.45
sm3 low-z	$2.0 \leq M_*/10^{10}\,{\rm M}_\odot < 4.0$	48 632	0.34 ± 0.10	3.47 ± 0.31	0.51 ± 0.07	0.99	-21.46	2.85
sm3 high-z	"	81 305	0.51 ± 0.08	2.44 ± 0.13	0.72 ± 0.05	0.98	-21.45	2.85
sm4 low-z	$4.0 \leq M_*/10^{10}\,{\rm M}_\odot < 8.0$	33 218	0.35 ± 0.09	4.05 ± 0.39	0.59 ± 0.08	0.99	-21.91	5.60
sm4 high-z	"	57 049	0.51 ± 0.08	2.72 ± 0.11	0.77 ± 0.04	0.99	-22.00	5.59
sm5 low-z	$8.0 \leq M_*/10^{10}\,{\rm M}_\odot < 16.0$	15 527	0.36 ± 0.08	5.00 ± 0.41	0.70 ± 0.07	1.00	-22.40	10.86
sm5 high-z	"	27 598	0.51 ± 0.08	3.56 ± 0.24	0.81 ± 0.07	1.00	-22.81	10.88
sm6 low-z	$16.0 \leq M_*/10^{10}\,{\rm M}_\odot < 32.0$	4605	0.36 ± 0.07	6.58 ± 0.50	1.51 ± 0.07	1.00	-23.00	21.13
sm6 high-z	"	7121	0.52 ± 0.07	4.18 ± 0.78	1.58 ± 0.16	1.00	-23.22	20.90
sm7 low-z	$32.0 \leq M_*/10^{10}\,{\rm M}_\odot < 64.0$	526	0.38 ± 0.06	8.89 ± 1.37	1.64 ± 0.15	1.00	-23.60	40.81
sm7 high-z	"	775	0.52 ± 0.07	5.61 ± 1.30	1.28 ± 0.21	1.00	-23.67	38.52
ETG low-z	$0 \leq$T_B$<2 \,|\, -23 \leq M_r < -21$	89 359	0.34 ± 0.10	3.43 ± 0.08	0.68 ± 0.02	0.99	-21.88	5.91
ETG high-z	"	137 144	0.51 ± 0.08	2.90 ± 0.09	0.83 ± 0.03	1.00	-21.91	5.74
LTG low-z	$2 \leq$T_B$<6 \,|\, -23 \leq M_r < -21$	30 926	0.35 ± 0.13	0.70 ± 0.13	0.87 ± 0.18	0.96	-21.64	1.73
LTG high-z	"	52 527	0.51 ± 0.10	1.33 ± 0.16	0.78 ± 0.11	0.99	-21.73	2.05
SOURCES	$0.65 \leq z_{\rm photo} < 1.2 \,|\, w > 0$	2926 894	0.93 ± 0.26	–	–	–	–	–

which have T_B<2, from late-type galaxies ('LTG').[1] In order to define a volume-limited sample of ETG and LTG, we select only luminous galaxies with rest-frame luminosities $-23 \leq M_r < -21$. With this luminosity cut, ETG and LTG are actually subsamples of L5 and L6 combined.

The stellar masses of the lenses are determined from the galaxy multi-colour data as described in section 2.1 of Velander et al. (2012). The estimators assume a Chabrier (2003) star initial mass function.

All three classes are further split into two photo-z bins: a 'low-z' bin with $0.2 \leq z_{\rm photo} < 0.44$ and a 'high-z' bin with $0.44 \leq z_{\rm photo} < 0.60$. As redshift estimators, we use the maximum probability redshifts of the redshift posterior provided by BPZ. The redshift boundaries give comparable numbers of lenses prior to attributing them to one of the three lens classes (Fig. 4). Not counting the high-z L1 and L2 samples, which have too faint limits to contain lenses,[2] we have in total 28 lens subsamples.

The true redshift distribution of a lens sample is not identical to the distribution of their photometric redshifts due to the errors in the photo-z estimators. For a magnitude cut of $i' < 22.5$, the errors are approximately $\sigma_z \lesssim 0.04(1+z)$ with a $\sim$3 per cent outlier rate (Hildebrandt et al. 2012). We combine the posterior redshift pdf of all lenses given by BPZ, see Fig. 5, to quantify the redshift uncertainties of complete lens samples. The depicted redshift probability distributions will be utilized when normalizing the G3L aperture statistics.

To help the comparison of our G3L results to future studies, we also quote the angular clustering and completeness of the lens samples. The results are listed in Table 1, the details are described in Appendices B1 (clustering) and B2 (completeness). In short, for the angular clustering of lenses, we approximate the angular galaxy two-point correlation function by a power law over the angular range $02 \leq \theta < 10$ arcmin. For each lens sample with the photo-z bin $[z_1, z_2]$, we quote the completeness factor $f_{\rm c}$ that expresses the

[1] Within BPZ values of T_B denote best-fitting galaxy templates: 1=CWW-Ell, 2=CWW-Sbc, 3=CWW-Scd, 4=CWW-Im, 5=KIN-SB3, and 6=KIN-SB2. Note that the templates are interpolated such that fractional numbers occur.

[2] Actually, we find a few galaxies in the high-z L1/L2 samples. These are probably extreme outliers with greatly inaccurate redshift estimates.

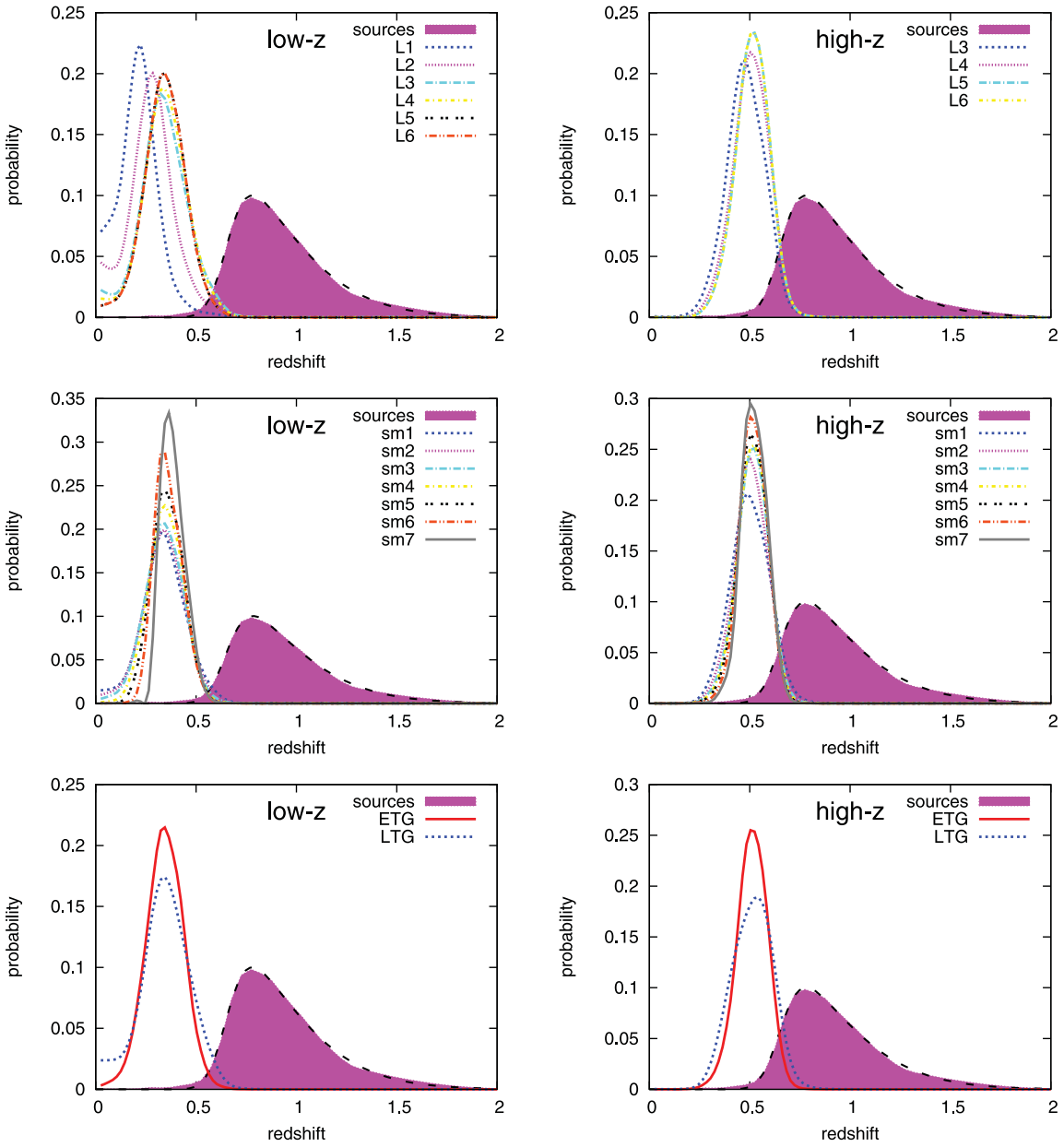

Figure 5. In contrast to Fig. 4, this figure shows the full BPZ redshift posterior of the various samples. Low-z lenses are selected from $z_{\rm photo} \in [0.2, 0.44]$, high-$z$ lenses from $z_{\rm photo} \in [0.44, 0.6]$ and sources from $z_{\rm photo} \in [0.65, 1.2]$. The dashed black line enclosing the source pdf is a parametrized fit, see Section 3.3 for best-fitting parameters.

average $V(z_1, z_{\rm max})/V(z_1, z_2)$ of all lenses in the sample; $V(z_1, z_2)$ is the light cone volume between redshift z_1 and z_2, and $z_{\rm max} \leq z_2$ is the maximum redshift up to which a lens is still above the flux limit $i' = 22.5$. A small $f_{\rm c}$ is a sign of a strong incompleteness because many galaxies similar to those observed near z_1 are presumably missing at higher redshifts. Due to the magnitude limit, samples containing a substantial portion of faint galaxies are most affected by incompleteness, most notably L1 and L2. As expected, the completeness drops if one moves from the low-z to the high-z bin in almost all cases. The few minor exceptions, L5 for instance, are probably due to shot noise in the $f_{\rm c}$ estimator. We conclude that L4–L6, sm3–sm7 and ETG/LTG are the most complete, volume-limited samples for our study ($f_{\rm c} > 0.80$ for both low-z and high-z). In Table 1, we also quote the average absolute r-band flux of the samples, listed as magnitude $\langle M_r \rangle$ and the their average stellar mass $\langle M_* \rangle$.

3.3 Source sample

All details concerning the galaxy shape measurement (employing the *lensfit* algorithm; Miller et al. 2007, 2012; Kitching et al. 2008), CFHTLenS source catalogue generation and the discussion of shear systematics are presented in Heymans et al. (2012) and Miller et al. (2012). We account for the multiplicative shear bias by employing the Miller et al. (2012) normalization scheme adjusted to our estimators (see Appendix A).

In order to reduce the level of undesired II- and GI-correlations in the measurements, we attempt to separate sources and lenses by redshift, utilizing photometric redshifts as estimators. As a compromize between accurate redshift estimates and a large numbers of sources, we apply a magnitude limit $i' < 24.7$ to the *lensfit* shear catalogue and select sources within $0.65 \leq z_{\rm photo} < 1.2$. As for the

lenses, the true redshift distribution is derived from the combined posterior redshift pdf of individual sources, shown in every panel of Fig. 5 in comparison to the redshift distribution of the lens samples. The individual posteriors are weighted with the source weight that is also used in the lensing analysis. The source redshift pdf is well fitted by a broken exponential distribution

$$p_{\rm b}(z) \propto \begin{cases} \exp\left(-p_0(z_0 - z)^{p_1}\right) & \text{if } z \leq z_0, \\ \exp\left(-p_2(z - z_0)^{p_3}\right) & \text{otherwise} \end{cases} \quad (33)$$

with fit parameters $p_0 = 91.14$, $p_1 = 2.623$, $p_2 = 4.093$, $p_3 = 1.378$ and $z_0 = 0.794$ (dashed black lines). With our selections, we find about 3×10^6 sources with mean redshift $\bar{z} \approx 0.93$. As can be seen in Fig. 5, the overlap of the various $p_{\rm f}(z)$ and the source $p_{\rm b}(z)$ is small but not entirely vanishing, mainly at $z = 0.5$–0.7 for the high-z and at $z \sim 0.6$ for the low-z samples. The typical overlapping area of the redshift probability distribution functions (visible in Fig. 5) is $\sim$12 per cent for the high-z samples and $\sim$4 per cent for the low-z samples.

4 RESULTS

4.1 Measurements and their uncertainties

In order to obtain measurements for the lensing aperture statistics, we use the method outlined in Section 2.3. As the binning grid for $\widetilde{\mathcal{G}}^{\rm est}$ and $\widetilde{G}_{\pm}^{\rm est}$, 100 log bins ranging between 9 arcsec and 50 arcmin are set up for $\vartheta_{1/2}$, 100 linear bins are used for the opening angle ϕ_3, yielding overall 10^6 bins with bin widths $\Delta\phi_3 = 3.6^\circ$ and $\Delta \ln \vartheta = 0.058$. All measurements are performed separately on every individual pointing, out of 129 square pointings with roughly 1 deg^2 each. Adjacent pointings partly overlap; however, which reduces the area that is actually used. In our study, we crop the pointings to remove the overlap. For the final result, individual estimates are combined by averaging the individual $\widetilde{\mathcal{G}}^{\rm est}$ and $\widetilde{G}_{\pm}^{\rm est}$ weighted by the number of triangles within each bin.

Finally, the combined estimates are transformed to the aperture statistics by the integral transformations discussed in SW05. In this way, the aperture statistics within $05 \leq \theta_{\rm ap} \leq 10$ arcmin for 10 aperture scale radii are computed. As addressed in Simon et al. (2008), the transformation from $\tilde{\mathcal{G}}$ or $\tilde{G}_{\pm}$ to aperture statistics becomes biased towards small and large aperture radii due to an insufficient sampling of the correlation functions. A similar transformation bias is also known for the aperture mass statistics (Kilbinger, Schneider & Eifler 2006). For the small separations, the bias depends in detail on the mean number density of the galaxies, most crucially the lenses, and the clustering of the lenses, which in combination determines the sampling of the correlation functions by small triangles. By comparison to simulated data, we made sure that this bias is negligible (below $\sim$10 per cent) within the range of $1 \lesssim \theta \lesssim 10$ arcmin in our case (see fig. 1 in Saghiha et al. 2012 for an illustration of the transformation bias). The variance of the measurements across all 129 pointings is used to estimate the covariance of measurement errors (Jackknifing; Appendix B1). The inverse covariance matrix is estimated from the pointing-to-pointing covariance according to the method in Hartlap, Simon & Schneider (2007).

4.2 E-mode measurements

Fig. 6 summarizes the E-mode results for the luminosity and stellar mass bins of the $\langle \mathcal{N}^2 M_{\rm ap} \rangle$ (top) and $\langle \mathcal{N} M_{\rm ap}^2 \rangle$ statistics (bottom). Due to the incompleteness in the samples, L1 and L2 are empty in the higher redshift bin and hence are missing in the corresponding plots. Likewise, due to the small number of lenses and correspondingly large error bars, also the data points of sm7 are missing. The signal dependence on galaxy type is displayed separately in Fig. 7. For aperture radii greater than $\sim$2 arcmin the measurements seem to be well approximated by power laws, which will be determined below. Below roughly 2 arcmin there are indications of deviations from the power-law behaviour at smaller radii in several cases, e.g. $\langle \mathcal{N}^2 M_{\rm ap} \rangle$ of low-z L1/L4, or $\langle \mathcal{N} M_{\rm ap}^2 \rangle$ of high-z L4/L6.

The result of $\langle \mathcal{N}^2 M_{\rm ap} \rangle$ of the LTG stand out as being the only one that is completely consistent with zero despite relatively small error bars. Therefore, the excess mass around LTG pairs vanishes within the statistical uncertainties. In strong contrast to that, the corresponding signal of the ETG sample is highly significant. From the LTG signal upper limit, we estimate the ETG signal to be greater by a factor of at least $\sim$10. This confirms the prediction of Saghiha et al. (2012) that is based on galaxy population synthesis models.

The low-z sample L1, with the fewest number of lenses, presumably is affected by the transformation bias. This can be seen by the clear drop of the data points for $\langle \mathcal{N}^2 M_{\rm ap} \rangle$ below $\theta_{\rm ap} \sim 2$ arcmin compared to a power-law behaviour at larger scales.

4.3 Systematics tests

General tests for systematics on the level of shear catalogue generation are to be found in Heymans et al. (2012). We only use CFHTLenS pointings that passed the therein described tests for cosmic shear applications. To further test for systematics in our measurements, we check for the consistency of the aperture statistics B- and P-modes with a null signal. The details of this test and, moreover, G3L measurements within separate CFHTLenS fields (W1–W4) are presented in Appendix C. The null test also allows us to quantify the significance of the signal in the E-mode channels of the statistics. Table 2 summarizes the tests for all statistics and galaxy samples.

In summary, we find that B/P-modes in the aperture statistics are consistent with zero between 1 and 10 arcmin. When looking at the combined L1–L6 sample, separate measurements within the survey fields W1–W4 agree well for both the low-z and the high-z redshift bin. This demonstrates the internal consistency of the data and that the observed signals do not originate from a single, possibly peculiar field. As to the E-mode channels of the statistics, we find for $\langle \mathcal{N}^2 M_{\rm ap} \rangle$ highly significant signals (95 per cent confidence) for all low-z samples, except for sm6 and sm7, and most high-z lens samples. Sm6 and sm7 pose exceptions because they contain relatively small numbers of galaxies. Apart from the high-z L3, L4 and sm4, all high-z sample measurements of $\langle \mathcal{N} M_{\rm ap}^2 \rangle$ are consistent with zero, whereas their low-z counterparts are mostly significant. As $\langle \mathcal{N} M_{\rm ap}^2 \rangle$ involves a three-point correlation function with two sources and one lens, the noise level of this measurement is naturally higher than for $\langle \mathcal{N}^2 M_{\rm ap} \rangle$.

5 INTERPRETATION

5.1 Lens-pair excess mass

Although aperture statistics and G3L correlators essentially contain the same information, we would like to show our $\mathcal{G}$-measurements for at least the ETG and LTG samples. As outlined in Simon et al. (2008) and Johnston (2006), the G3L correlation function $\mathcal{G}$ can conveniently be interpreted as a convergence map (excess mass map) once the separation of the two lenses is fixed; the E-mode in

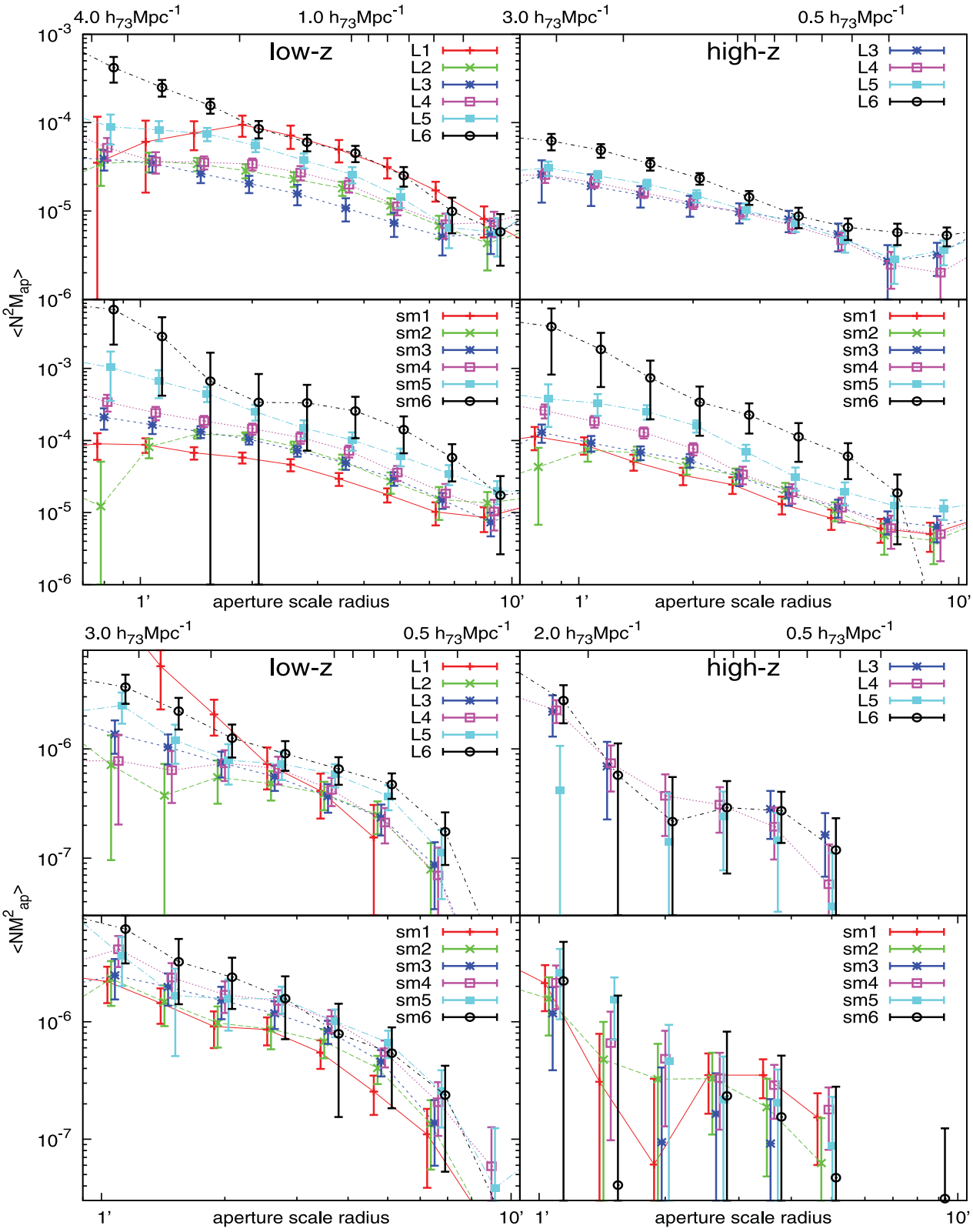

Figure 6. Measurements of the E-mode aperture statistics $\langle \mathcal{N}^2 M_{\rm ap}\rangle(\theta)$ (top figure) and $\langle \mathcal{N} M_{\rm ap}^2\rangle(\theta)$ (bottom figure) as a function of aperture scale radius θ. The left-hand column depicts measurements for the low-z bin, the right-hand column the high-z bin. Different lines refer to different lens samples (Table 1). Note that the values get biased for $\theta \lesssim 1$ arcmin due to the transformation bias. The error bars indicate the 1σ standard deviation of the mean of all pointings considered. The missing data points are outside the plotting range but consistent with zero. The numbers at the top indicate the effective scale of the statistics according to the maximum in the u-filter. L1–L6: M_r-luminosities increasing from -17.8 mag to -22.4 mag; sm1–sm6: increasing stellar masses from 7×10^9 $M_\odot$ to 2×10^{11} $M_\odot$.

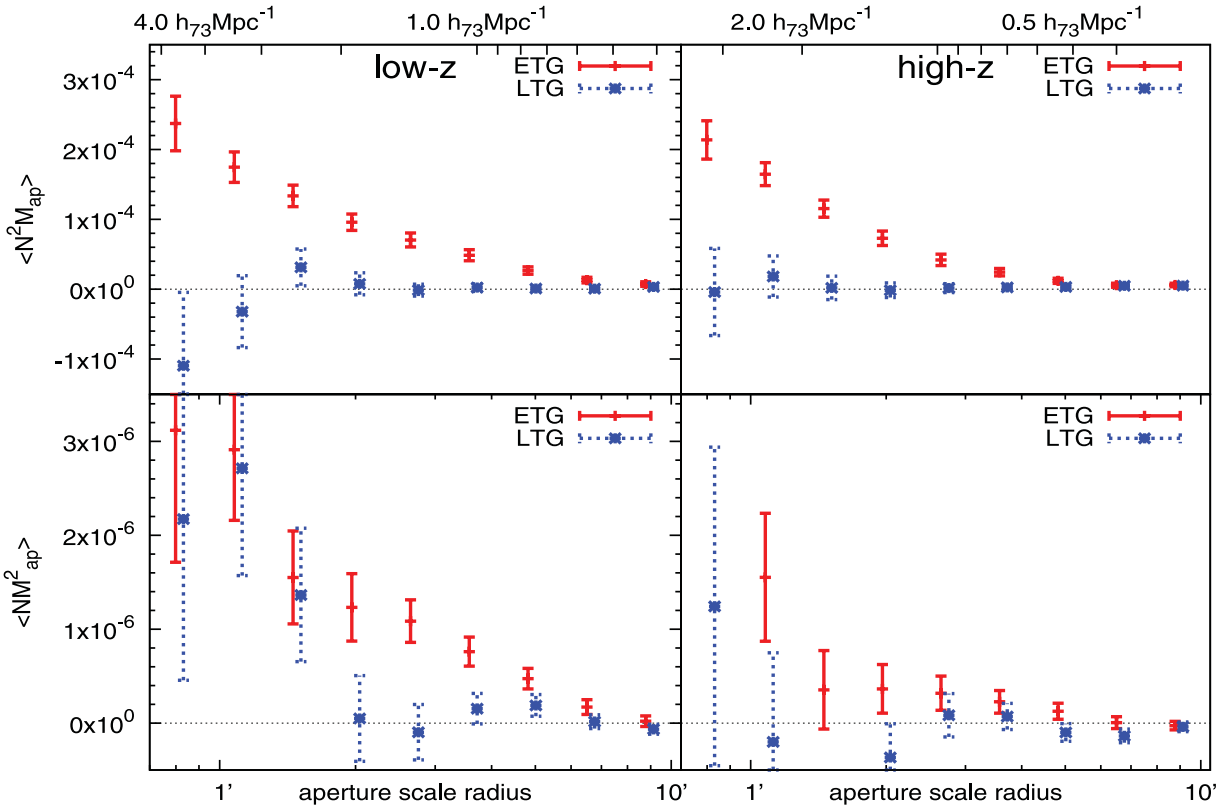

Figure 7. Aperture statistics results for the late-type and early-type lens samples. The left-hand column shows the low-z redshift bin, the right-hand column the high-z redshift bin. Top row and bottom row correspond to $\langle\mathcal{N}^2 M_{\rm ap}\rangle$ and $\langle\mathcal{N}M_{\rm ap}^2\rangle$, respectively. The numbers at the top indicate the effective scale according to the maximum in the u-filter. ETG: early-type galaxies; LTG: late-type galaxies.

Table 2. Results of the null tests for the different channels of the statistics. The quoted values are the reduced $\Delta\chi^2$ with d.o.f. = 7. for the E-modes and P-mode, $\langle\mathcal{N}^2 M_\perp\rangle$, and d.o.f. = 14 for the combined B/P-mode, $\langle\mathcal{N}M_\perp^2\rangle$ and $\langle\mathcal{N}M_\perp M_{\rm ap}\rangle$. E-modes consistent with a null signal are in bold, P- or P/B-modes inconsistent with a null signal are underlined. The adopted confidence levels are 95 per cent. Only data points within the range $15 \le \theta < 10$ arcmin were used for this test.

	$0.22 \le z_{\rm photo} < 0.44$				$0.44 \le z_{\rm photo} < 0.60$			
	$\langle\mathcal{N}^2 M_{\rm ap}\rangle$		$\langle\mathcal{N}M_{\rm ap}^2\rangle$		$\langle\mathcal{N}^2 M_{\rm ap}\rangle$		$\langle\mathcal{N}M_{\rm ap}^2\rangle$	
Sample	E-mode	P-mode	E-mode	P/B-mode	E-mode	P-mode	E-mode	P/B-mode
L1	3.22	1.27	2.64	1.24	–	–	–	–
L2	7.32	1.57	2.31	1.75	–	–	–	–
L3	3.79	0.66	4.93	0.75	3.21	0.94	2.38	1.22
L4	9.26	0.58	2.62	1.14	7.66	0.89	2.38	0.79
L5	6.72	1.00	4.31	0.80	7.08	1.95	**0.81**	1.06
L6	7.76	0.99	4.92	0.74	7.07	1.50	**1.74**	0.41
sm1	6.41	1.06	4.06	1.55	5.18	0.74	**1.90**	0.68
sm2	12.43	0.59	3.55	1.11	5.97	0.40	**0.95**	0.83
sm3	7.07	0.99	4.05	0.76	5.62	0.65	**0.18**	1.19
sm4	7.64	1.86	4.83	0.58	5.93	0.27	2.28	1.12
sm5	3.76	1.27	4.95	0.52	6.74	1.18	**0.78**	0.96
sm6	**0.65**	0.91	**1.15**	1.00	2.33	0.68	**0.64**	1.42
sm7	**0.93**	1.16	**0.66**	1.61	**0.45**	0.42	**1.52**	1.87
ETG	12.50	0.87	6.62	0.65	15.24	1.74	**1.21**	1.06
LTG	**0.77**	0.85	**1.58**	1.52	**0.90**	1.20	**1.45**	0.37

$\mathcal{G}$ is a series of such maps for varying lens–lens separations. After a rotation, the correlator $\bar{\mathcal{G}}$ is a stacked shear field around the lens pair, from which we subtract off the GGL signal around the individual lenses to determine the connected part $\mathcal{G}$. To obtain the excess mass maps for the ETG and LTG in Fig. 8, we transform this stacked shear field to a convergence map utilizing the algorithm in Kaiser & Squires (1993). For these maps, we consider relatively small lens–lens separations between 40 and 60 arcsec as in Simon et al. (2008), and we combine the maps of the low-z and high-z samples; lens–lens-source triangles are rescaled inside the map such that lenses

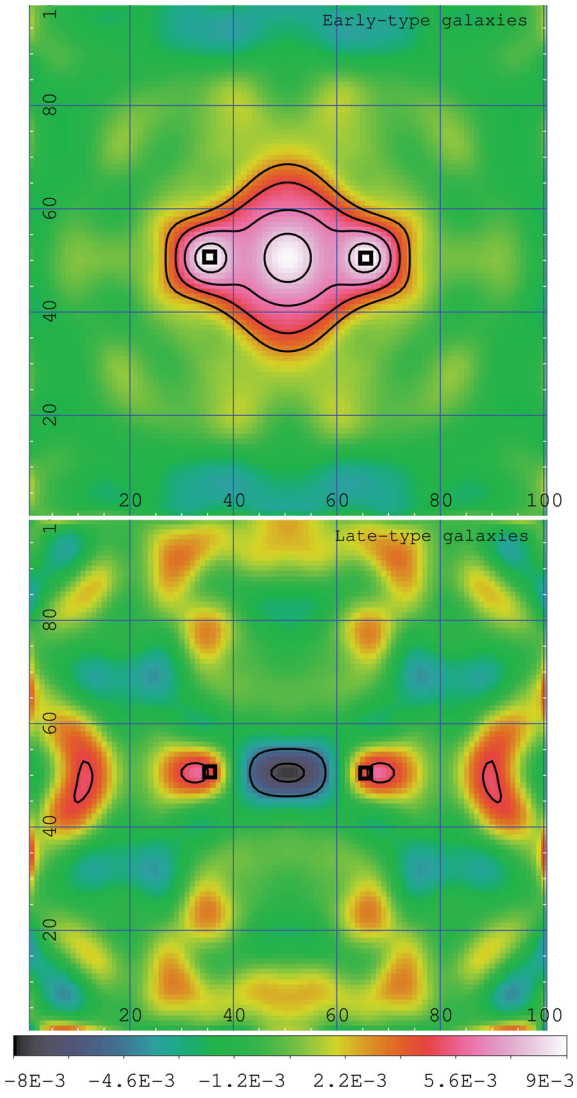

Figure 8. Visualization of the $\mathcal{G}$-measurement. Shown is the excess mass $\langle\kappa_g(\boldsymbol{\theta}_1)\kappa_g(\boldsymbol{\theta}_2)\kappa(\boldsymbol{\theta}_3)\rangle$ (intensity scale) as function of $\boldsymbol{\theta}_3$ around early-type (*top*) and late-type galaxy pairs (*bottom*) with mean angular separations $|\boldsymbol{\theta}_1 - \boldsymbol{\theta}_2|$ between 40 and 60 arcsec; one map pixel corresponds to 1.67 arcsec (x- and y-axis labels). The lens positions $\boldsymbol{\theta}_1, \boldsymbol{\theta}_2$ are indicated as boxes, the contours show the S/N levels 2, 3, ... (positive excess mass) and −3,−2 (negative excess mass). To increase the signal-to-noise ratio the low-z and high-z maps of the ETG and LTG samples have been combined. A smoothing with a Gaussian kernel of rms size 6.7 arcsec has been applied to map.

are always at the same position in the map (boxes). We also exploit the parity invariance of the maps by averaging the left and right half of the map, thereby increasing the signal-to-noise ratio, see Simon et al. (2008) for details.

The ETG map contains more significant structure and higher convergence values compared to the LTG map, which has only a weak signal. Qualitatively, the excess mass of the ETG sample is concentrated between the lens pair, whereas the LTG lenses seem to possess a small halo of excess mass around the individual lenses and a convergence trough between them. The latter implies that the average convergence about a LTG pair (both lenses at similar distance) at given separation is lower than the sum of convergence around two mean individual LTG. We will study these maps in more detail in a forthcoming paper and focus on the aperture statistics for the remainder of this paper.

5.2 Power-law fits to measurements

For aperture scale radii larger than $\theta \gtrsim 2$ arcmin, our measurements are reasonably consistent with a simple power law. Therefore, we fit power laws $\langle\mathcal{N}^n M_{\rm ap}^m\rangle(\theta_{\rm ap}) = A_0(\theta/1\,\text{arcmin})^{-\alpha}$ to data points within $15 \leq \theta < 10$ arcmin to quantify the measured profiles of the statistics $n = 2, m = 1$ and $n = 1, m = 2$, see Table 3. The fit starts at 1.5 arcmin in order not to be too strongly influenced by the transformation bias. Fits use the Jackknife covariance matrices based on the measurements in the different pointings, as in equation (B2). For the fit, a multivariate Gaussian noise model for the measurement errors is adopted. The quoted values indicate the posterior median and a 68 per cent credibility region about the median for the amplitude A_0 and slope α. The posterior adopts a top-hat prior for the power-law slope, only allowing values within $\alpha \in [0, 5]$.

Fig. 9 depicts the dependence of the slope α on the lens M_r-magnitude and stellar mass for $\langle\mathcal{N}^2 M_{\rm ap}\rangle$ of all samples with at least a 95 per cent confidence detection (Table 2). We find a clear trend towards steeper slopes (steeper equilateral bispectra) for more luminous galaxies and galaxies with higher stellar mass. Note that sm6 and sm7 contain on average galaxies more luminous than those of L5 and L6 (Table 1). The figure also depicts the measured slopes for the ETG samples, which are consistent with the L-subsamples of comparable M_r-luminosity (between L5 and L6). Slopes weakly constrained by the data have posterior medians that are drawn towards the centre of the top-hat prior, $\alpha = 2.5$. This mainly applies to the noisier $\langle\mathcal{N} M_{\rm ap}^2\rangle$ measurements, for which reason they are not included in Fig. 9 but are listed in Table 3.

5.3 Normalized measurements

The G3L aperture statistics are directly related to the 3D matter–galaxy cross-bispectra and the redshift distribution of lenses and sources (Section 2.4). The radial galaxy distributions and the fiducial cosmology define a smoothing kernel in radial and transverse direction. To disentangle, to the lowest order, the dependence of the signal on the physically relevant bispectrum from the dependence on source or lens distribution, we introduce a normalization scheme.

Combining equation (19) and equation (23) shows that $\langle\mathcal{N}^2 M_{\rm ap}\rangle$ constitutes a radially and transversely weighted average of the 3D bispectrum $B_{\rm ggm}(\boldsymbol{k}_1, \boldsymbol{k}_2, \chi)$, namely

$$\begin{aligned}\langle\mathcal{N}^2 M_{\rm ap}\rangle(\theta_1;\theta_2;\theta_3) =& \\ \frac{3\Omega_{\rm m}}{2D_{\rm H}^2}\int_0^{\chi_{\rm H}} {\rm d}\chi\, \frac{g(\chi)p_{\rm f}^2(\chi)}{f_{\rm K}^3(\chi)a^2(\chi)} \int \frac{{\rm d}^2\ell_1 {\rm d}^2\ell_2 {\rm d}^2\ell_3}{(2\pi)^6}& \\ \times\, \tilde{u}(\ell_1\theta_1)\tilde{u}(\ell_2\theta_2)\tilde{u}(\ell_3\theta_3)& \\ \times\, (2\pi)^2\delta_{\rm D}(\boldsymbol{\ell}_1+\boldsymbol{\ell}_2+\boldsymbol{\ell}_3) B_{\rm ggm}\left(\frac{\boldsymbol{\ell}_1}{f_{\rm K}(\chi)}, \frac{\boldsymbol{\ell}_2}{f_{\rm K}(\chi)}, \chi\right)&\,. \end{aligned} \tag{34}$$

By changing the integration variables as in $\boldsymbol{\ell}_i = f_{\rm K}(\chi)\boldsymbol{k}_i$ we write this integral as

$$\begin{aligned}\langle\mathcal{N}^2 M_{\rm ap}\rangle(\theta_1;\theta_2;\theta_3) =:& \\ \int_0^{\chi_{\rm h}} {\rm d}\chi\, q_{\rm ggm}(\chi)\overline{B}_{\rm ggm}\left(\frac{1}{f_{\rm K}(\chi)\theta_1}, \frac{1}{f_{\rm K}(\chi)\theta_2}, \frac{1}{f_{\rm K}(\chi)\theta_3}, \chi\right)&\,, \end{aligned} \tag{35}$$

Table 3. Power-law fits $\langle \mathcal{N}^n M_{\rm ap}^m \rangle(\theta) = A_0(\theta/1')^{-\alpha}$ to the measured aperture statistics in Fig. 6; A_0 is the signal amplitude at an aperture scale radius of $\theta = 1$ arcmin. The fit considers only data within $\theta \in$ [15 arcmin, 10 arcmin]. The quoted errors bracket a 68 per cent credibility region about the median.

	$0.20 \le z_{\rm photo} < 0.44$				$0.44 \le z_{\rm photo} < 0.60$			
	$\langle \mathcal{N}^2 M_{\rm ap} \rangle$		$\langle \mathcal{N} M_{\rm ap}^2 \rangle$		$\langle \mathcal{N}^2 M_{\rm ap} \rangle$		$\langle \mathcal{N} M_{\rm ap}^2 \rangle$	
Sample	$A_0/10^{-5}$	α	$A_0/10^{-7}$	α	$A_0/10^{-5}$	α	$A_0/10^{-7}$	α
L1	$10.57^{+5.12}_{-4.90}$	$1.40^{+0.90}_{-0.34}$	$54.38^{+25.92}_{-20.06}$	$2.59^{+0.94}_{-0.59}$	–	–	–	–
L2	$5.15^{+1.05}_{-0.99}$	$1.04^{+0.18}_{-0.16}$	$9.48^{+8.30}_{-11.37}$	$2.11^{+1.59}_{-0.73}$	–	–	–	–
L3	$3.66^{+1.04}_{-0.98}$	$1.05^{+0.31}_{-0.24}$	$28.22^{+7.95}_{-6.63}$	$1.87^{+0.44}_{-0.29}$	$8.56^{+3.78}_{-2.75}$	$1.66^{+0.84}_{-0.41}$	$41.07^{+27.18}_{-21.95}$	$3.84^{+0.71}_{-1.06}$
L4	$5.10^{+1.04}_{-0.95}$	$0.97^{+0.20}_{-0.17}$	$16.76^{+8.95}_{-6.88}$	$1.95^{+1.14}_{-0.51}$	$6.85^{+1.50}_{-1.34}$	$1.49^{+0.29}_{-0.23}$	$31.90^{+18.06}_{-13.26}$	$3.30^{+0.95}_{-0.87}$
L5	$12.30^{+2.47}_{-2.33}$	$1.44^{+0.23}_{-0.18}$	$34.56^{+14.41}_{-10.48}$	$1.99^{+0.80}_{-0.37}$	$9.15^{+1.80}_{-1.70}$	$1.50^{+0.26}_{-0.20}$	$-8.89^{+14.23}_{-18.56}$	$3.58^{+0.88}_{-1.33}$
L6	$35.54^{+9.15}_{-7.80}$	$1.91^{+0.35}_{-0.26}$	$62.85^{+25.33}_{-18.24}$	$2.10^{+0.58}_{-0.36}$	$19.89^{+6.28}_{-5.48}$	$1.68^{+0.31}_{-0.30}$	$42.07^{+29.43}_{-21.14}$	$3.43^{+0.93}_{-1.02}$
sm1	$11.95^{+2.57}_{-2.42}$	$1.29^{+0.22}_{-0.18}$	$42.70^{+19.94}_{-12.91}$	$2.16^{+0.95}_{-0.46}$	$9.34^{+4.01}_{-2.94}$	$1.55^{+0.52}_{-0.34}$	$28.69^{+28.52}_{-20.40}$	$3.55^{+0.91}_{-1.26}$
sm2	$19.91^{+3.09}_{-2.96}$	$1.24^{+0.17}_{-0.14}$	$38.15^{+16.87}_{-12.24}$	$1.90^{+0.82}_{-0.39}$	$14.48^{+3.63}_{-3.22}$	$1.72^{+0.33}_{-0.23}$	$25.94^{+22.36}_{-18.47}$	$3.50^{+0.89}_{-1.08}$
sm3	$24.49^{+5.22}_{-4.91}$	$1.54^{+0.18}_{-0.16}$	$45.06^{+16.95}_{-14.01}$	$2.09^{+0.85}_{-0.36}$	$11.11^{+3.28}_{-3.00}$	$1.39^{+0.26}_{-0.24}$	$-4.83^{+16.48}_{-19.77}$	$3.52^{+0.91}_{-1.30}$
sm4	$34.96^{+6.88}_{-6.40}$	$1.65^{+0.25}_{-0.19}$	$61.43^{+19.67}_{-16.56}$	$1.95^{+0.51}_{-0.29}$	$26.16^{+5.84}_{-5.50}$	$2.10^{+0.32}_{-0.24}$	$31.46^{+22.60}_{-16.94}$	$3.10^{+1.04}_{-0.88}$
sm5	$87.19^{+33.76}_{-25.14}$	$1.87^{+0.65}_{-0.27}$	$77.89^{+26.49}_{-22.99}$	$1.96^{+0.45}_{-0.29}$	$47.34^{+14.86}_{-13.26}$	$1.79^{+0.24}_{-0.24}$	$63.93^{+46.24}_{-35.21}$	$3.61^{+0.82}_{-1.03}$
sm6	$197.06^{+313.36}_{-347.35}$	$3.60^{+0.84}_{-1.02}$	$124.38^{+83.56}_{-64.46}$	$3.21^{+1.00}_{-0.91}$	$400.32^{+212.89}_{-189.83}$	$3.68^{+0.72}_{-0.73}$	$53.51^{+88.69}_{-68.50}$	$3.71^{+0.81}_{-1.25}$
sm7	$315.06^{+307.91}_{-274.91}$	$3.26^{+1.04}_{-1.32}$	$230.78^{+265.46}_{-198.85}$	$3.81^{+0.74}_{-1.19}$	$-136.21^{+521.62}_{-483.19}$	$3.14^{+1.08}_{-1.15}$	$407.91^{+307.45}_{-276.37}$	$4.09^{+0.57}_{-1.11}$
ETG	$23.27^{+3.05}_{-2.97}$	$1.49^{+0.16}_{-0.13}$	$41.94^{+10.22}_{-9.29}$	$1.71^{+0.29}_{-0.21}$	$21.51^{+2.85}_{-2.74}$	$1.72^{+0.19}_{-0.16}$	$19.73^{+16.79}_{-12.41}$	$3.03^{+1.12}_{-1.03}$
LTG	$10.82^{+13.05}_{-10.46}$	$3.64^{+0.82}_{-1.16}$	$59.49^{+42.99}_{-35.02}$	$3.86^{+0.70}_{-1.04}$	$3.25^{+5.85}_{-4.51}$	$2.81^{+1.36}_{-1.52}$	$-26.87^{+18.66}_{-23.95}$	$3.41^{+0.94}_{-1.19}$

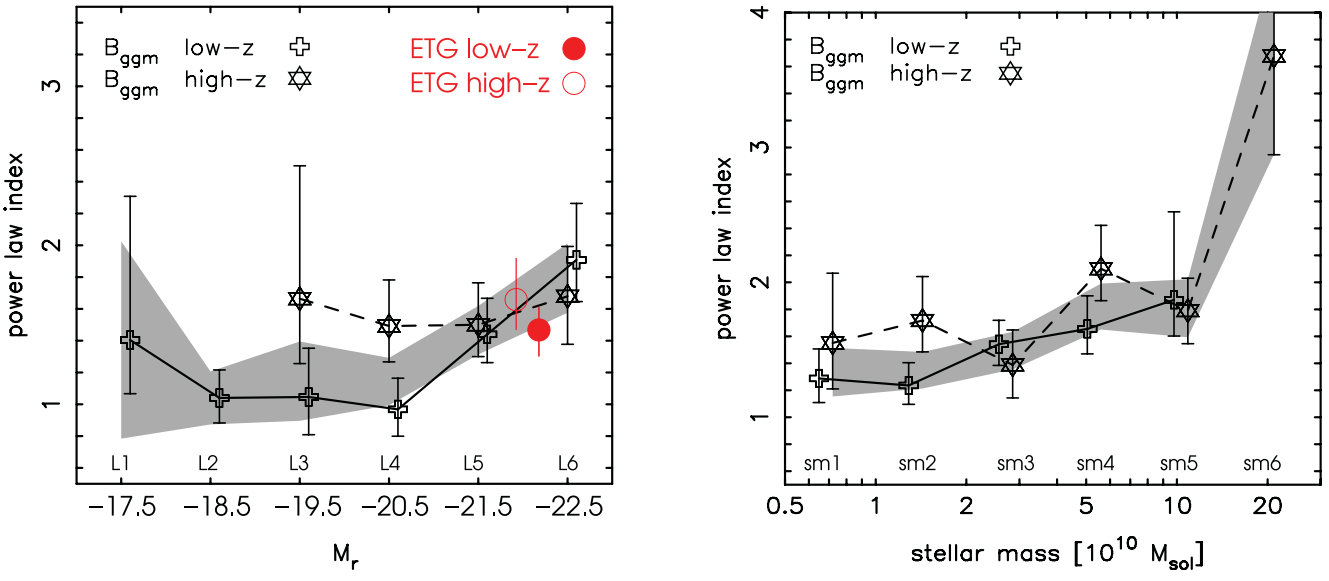

Figure 9. Dependence of the power-law index α in the normalized aperture statistics $\langle \mathcal{N}^2 M_{\rm ap} \rangle$ within $15 \le \theta < 10$ arcmin with M_r-band magnitude (left-hand panel) and stellar mass of lenses (right-hand panel). Table 3 lists the power-law indices of all statistics. Only fits to measurements with a 95 per cent confidence detection are plotted. The shaded region highlights the 68 per cent credibility region of the combined low-z (open crosses) and high-z (open stars). Also shown are the slopes for the early-type galaxy sample in the corresponding magnitude range (left-hand panel). For clarity, these data points are offset about their actual mean $\langle M_r \rangle = -21.88(-21.91)$ for the low-z (high-z) sample.

for which we introduce the u-filtered bispectrum

$$\overline{B}_{\rm ggm}\left(\frac{1}{R_1}, \frac{1}{R_2}, \frac{1}{R_3}, \chi\right) := \int \frac{{\rm d}^2k_1 {\rm d}^2k_2}{(2\pi)^4 D_{\rm H}^2} \left(\tilde{u}(k_1 R_1)\tilde{u}(k_2 R_2)\tilde{u}(|\boldsymbol{k}_1 + \boldsymbol{k}_2| R_3) B_{\rm ggm}(\boldsymbol{k}_1, \boldsymbol{k}_2, \chi)\right). \quad (36)$$

As implied by (35), the lensing aperture statistics are basically the transversely u-filtered bispectrum $\overline{B}_{\rm ggm}$ averaged in radial direction by the kernel $q_{\rm ggm}(\chi)$. For equally sized aperture radii $\theta_1 = \theta_2 = \theta_3$, the u-filter gives most weight to the equilateral bispectrum $B_{\rm ggm}(\boldsymbol{k}_1, \boldsymbol{k}_2, \chi)$ with $k_1 = k_2 = |\boldsymbol{k}_1 + \boldsymbol{k}_2|$, but also mixes in other triangle configurations to some degree. The radial weighting kernel,

$$q_{\rm ggm}(\chi) := \frac{3\Omega_{\rm m}}{2} \frac{g(\chi) p_{\rm f}^2(\chi) f_{\rm K}(\chi)}{a(\chi)}, \quad (37)$$

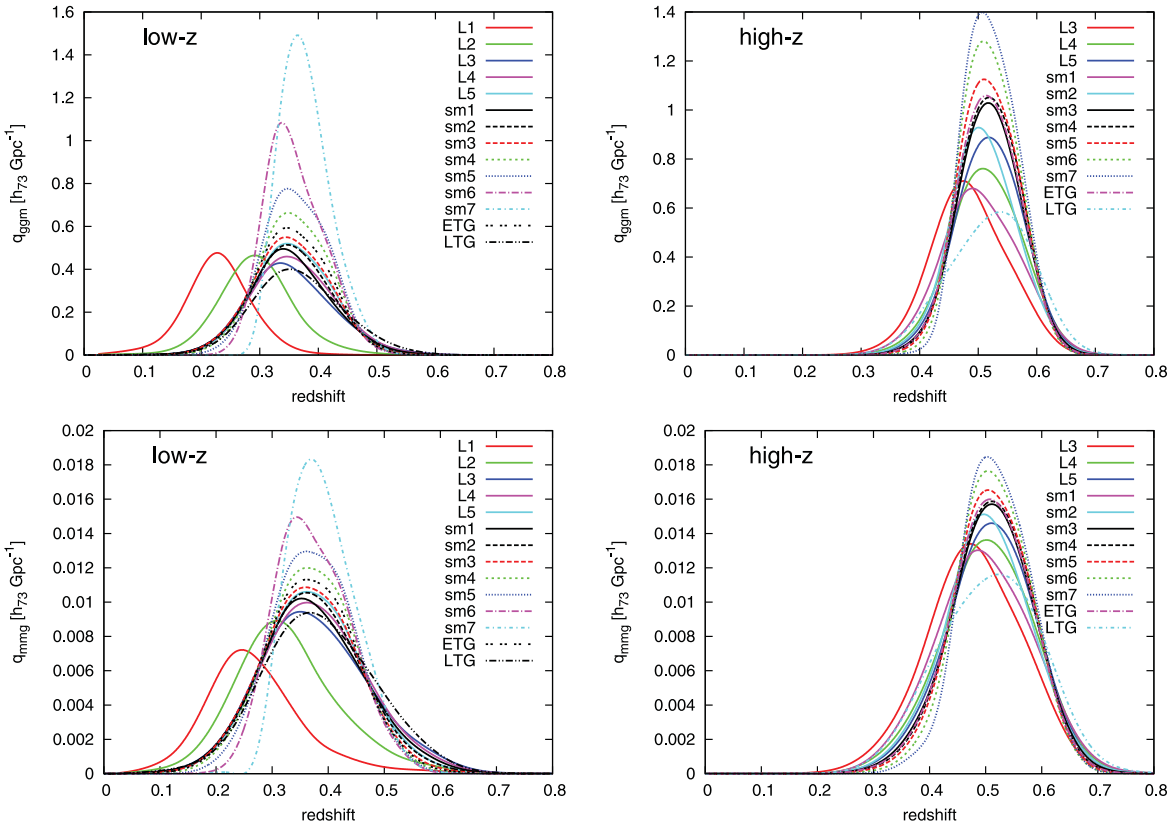

Figure 10. Radial weight of the matter–galaxy bispectrum for the different lens samples used in this study: $\langle\mathcal{N}^2 M_{\rm ap}\rangle$ (top row) and $\langle\mathcal{N}M_{\rm ap}^2\rangle$ (bottom row). The left-hand column is for lenses with $z_{\rm photo} \in [0.2, 0.44]$ (low-z), the right-hand column for $z_{\rm photo} \in [0.44, 0.6]$ (high-z). L1–L6: M_r-luminosities increasing from -17.8 mag to -22.4 mag; sm1–sm7: increasing stellar masses from 7×10^9 $M_\odot$ to 4×10^{11} $M_\odot$; ETG: early-type galaxies; LTG: late-type galaxies.

is peaked at a radial distance $\chi_{\rm max}$ that is determined by the redshift pdf of lenses and sources (top row of Fig. 10). Therefore, most weight is given to the bispectrum at distance $\chi_{\rm max}$.

The kernel $q_{\rm ggm}(\chi)$ is not normalized, i.e. $\int {\rm d}\chi\, q_{\rm ggm}(\chi) \neq 1$, such that the aperture statistics assume a value that depends not only on the underlying 3D bispectrum $B_{\rm ggm}$ but also on the normalization. In order to make measurements comparable for different lens and source samples, we define a normalized statistic $\mathcal{B}_{\rm ggm}$ through the relation

$$\langle\mathcal{N}^2 M_{\rm ap}\rangle(\theta_1;\theta_2;\theta_3) = \mathcal{B}_{\rm ggm}(R_1, R_2, R_3) \int_0^{\chi_{\rm h}} {\rm d}\chi\, q_{\rm ggm}(\chi) \qquad (38)$$

with $R_i := f_{\rm K}(\chi_{\rm max})\theta_i$. We emphasize that by this definition $\mathcal{B}_{\rm ggm}$ is not a deprojection of the angular aperture statistics to the spatial 3D bispectrum. This would involve the inversion of the χ-integral. Instead we, in effect, normalize the statistic by the area $\int {\rm d}\chi\, q_{\rm ggm}(\chi)$, and we convert angular scales to projected physical scales through the angular diameter distance $f_{\rm K}(\chi_{\rm max})$ at maximum weight $q_{\rm ggm}(\chi_{\rm max})$.

The same line of reasoning can be applied to the second G3L aperture statistics for which we obtain

$$\langle\mathcal{N}M_{\rm ap}^2\rangle(\theta_1;\theta_2;\theta_3) = \mathcal{B}_{\rm mmg}(R_1, R_2, R_3) \int_0^{\chi_{\rm h}} {\rm d}\chi\, q_{\rm mmg}(\chi)\,, \qquad (39)$$

with its own radial filter

$$q_{\rm mmg}(\chi) := \frac{9\Omega_{\rm m}^2}{4D_{\rm H}^2} \frac{g^2(\chi) p_{\rm f}(\chi) f_{\rm K}^2(\chi)}{a^2(\chi)}\,. \qquad (40)$$

Examples of kernels $q_{\rm mmg}(\chi)$ relevant for this work are depicted in the bottom row of Fig. 10.

By definition the aperture statistics $\langle\mathcal{N}^n M_{\rm ap}^m\rangle$, as moments of smoothed density contrasts on the sky, are dimensionless. As $q_{\rm ggm}(\chi)$ has the dimension [length^{-1}], equation (37), we deduce from equation (35) that the u-filtered $\mathcal{B}_{\rm ggm}$ is also dimensionless. This becomes also obvious from equation (38) because the normalization integral is dimensionless. A similar argument applies to the dimensionless $\mathcal{B}_{\rm mmg}$.

In our analysis, we estimate the equilateral $\mathcal{B}_{\rm ggm}$ or $\mathcal{B}_{\rm mmg}$ amplitudes of all samples at a common comoving length scale of $R_i = R_{1\rm Mpc} = 1\,h_{100}^{-1}$ Mpc (or $k \approx \sqrt{2}/R_{1\rm Mpc} \sim 1.4\,h_{100}\,{\rm Mpc}^{-1}$ for the exponential u-filter). For this purpose, the power-law fits in Table 3 to the aperture statistics are employed, which essentially describe the data at the scales of interest, to interpolate in the case of $\mathcal{B}_{\rm ggm}$

$$\mathcal{B}_{\rm ggm}(R) := \mathcal{B}_{\rm ggm}(R, R, R) = \underbrace{\frac{A_0}{\int_0^{\chi_{\rm h}} {\rm d}\chi\, q_{\rm ggm}(\chi)} \left(\frac{f_{\rm K}(\chi_{\rm max}) \times 1'}{h_{100}^{-1}\,{\rm Mpc}}\right)^{+\alpha}}_{=:\mathcal{B}_{\rm ggm}(R_{1\,\rm Mpc})} \left(\frac{R}{h_{100}^{-1}\,{\rm Mpc}}\right)^{-\alpha}. \qquad (41)$$

We are quoting only the amplitude $\mathcal{B}_{\rm ggm}(R_{1\rm Mpc})$ in the following. Likewise for the matter–matter–galaxy bispectrum $\mathcal{B}_{\rm mmg}$ we have

$$\mathcal{B}_{\rm mmg}(R) := \mathcal{B}_{\rm mmg}(R, R, R) = \underbrace{\frac{A_0}{\int_0^{\chi_{\rm h}} {\rm d}\chi\, q_{\rm mmg}(\chi)} \left(\frac{f_{\rm K}(\chi_{\rm max}) \times 1'}{h_{100}^{-1}\,{\rm Mpc}}\right)^{+\alpha}}_{=:\mathcal{B}_{\rm mmg}(R_{1\,\rm Mpc})} \left(\frac{R}{h_{100}^{-1}\,{\rm Mpc}}\right)^{-\alpha}. \qquad (42)$$

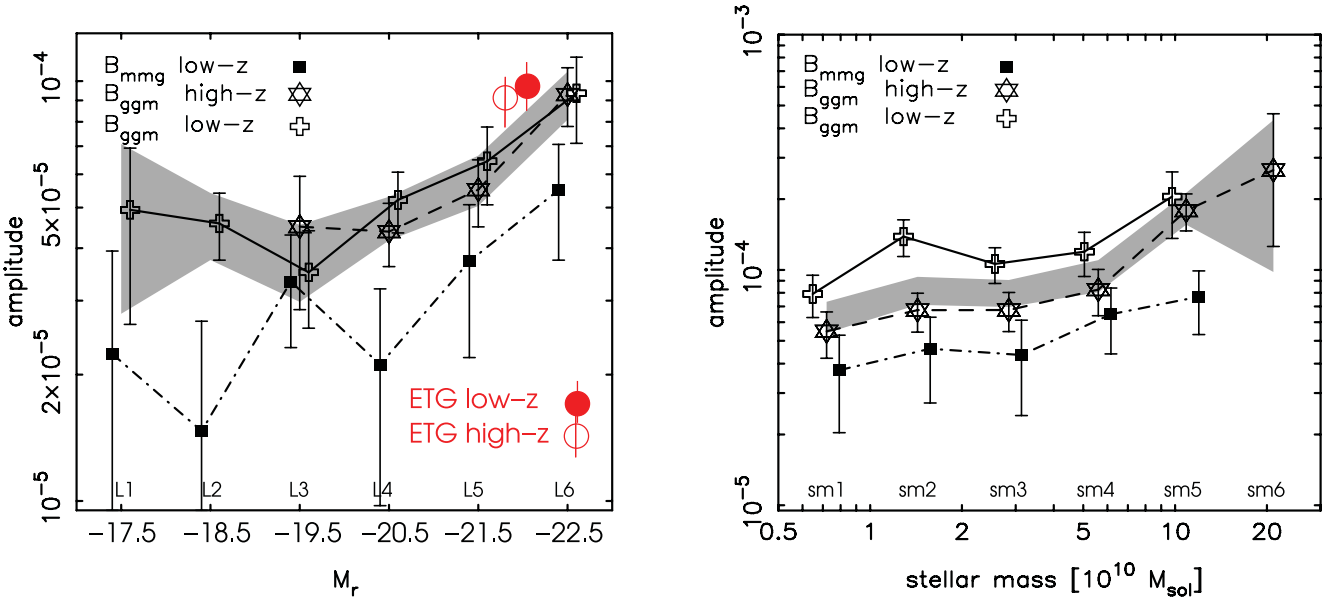

Figure 11. Trends of the (significant) galaxy–matter bispectra $\mathcal{B}_{\rm mmg}(R)$ and $\mathcal{B}_{\rm ggm}(R)$ for $k = \sqrt{2}/R = 1.03\,h_{73}\,{\rm Mpc}^{-1}$ with function of M_r-luminosity (left-hand panel) and stellar mass (right-hand panel). Shown are both redshift bins together. The left-hand panel also includes $\mathcal{B}_{\rm ggm}(R)$ data points of the early-type galaxy sample. These data points are somewhat offset with respect to their actual mean $\langle M_r\rangle = -21.88(-21.91)$ (high-z in brackets) for clarity. The shaded area highlights the 1σ constraints of $\mathcal{B}_{\rm ggm}(R)$ for low-z and high-z combined.

To assess the uncertainty in the bispectrum amplitude, we marginalize over the uncertainties in A_0, the aperture statistics amplitude at 1 arcmin, and α, the power-law index, taking into account the correlation of their errors. A value of $R_{\rm 1Mpc}$ corresponds to an aperture scale radius between 2.5 to 3.5 arcmin depending on the mean redshift of the lens samples. The compiled results are plotted in Fig. 11 – one of the main results of our study – to highlight the trends with M_r-magnitude and stellar mass. As before, only measurements with highly significant detections are included in the plot.

At the corresponding M_r-magnitude range, we include also the normalized $\langle\mathcal{N}^2 M_{\rm ap}\rangle$ amplitude of the ETG sample. Their amplitude is somewhat higher in comparison to L5 and L6. This can be explained by the fact that the LTG sample is included in the L samples but not in the ETG sample of similar luminosity: the LTG have a normalized amplitude considerably smaller than that of the ETG.

5.4 Third-order galaxy biasing

SW05 introduced a set of third-order galaxy biasing parameters b_3, r_1, r_2 to parametrize the galaxy–matter bispectra relative to the matter bispectrum $B_{\rm mmm}$,

$$B_{\rm ggm}(\boldsymbol{k}_1, \boldsymbol{k}_2, \chi) = b_3^2 r_2\, B_{\rm mmm}(\boldsymbol{k}_1, \boldsymbol{k}_2, \chi)\,, \tag{43}$$

$$B_{\rm mmg}(\boldsymbol{k}_1, \boldsymbol{k}_2, \chi) = b_3 r_1\, B_{\rm mmm}(\boldsymbol{k}_1, \boldsymbol{k}_2, \chi)\,. \tag{44}$$

The coefficients b_3, r_1, r_2 are also functions of $\boldsymbol{k}_1, \boldsymbol{k}_2, \chi$, which have been omitted here to save space. For galaxies faithfully tracing the underlying matter distribution one finds $r_1 = r_2 = b_3 = 1$ for all scales. This parametrization generalizes the earlier similar second-order galaxy bias parametrization (e.g. Tegmark & Bromley 1999; Hoekstra et al. 2002; Pen et al. 2003) to the third-order. Our normalized G3L measurements of $\mathcal{B}_{\rm ggm}(R)$ and $\mathcal{B}_{\rm mmg}(R)$ can be utilized to constrain the ratio $r_1/(r_2 b_3)$ for a physical scale R by considering the combined statistics

$$\Psi(R) := \frac{\mathcal{B}_{\rm mmg}(R)}{\mathcal{B}_{\rm ggm}(R)} = \frac{\int_0^{\chi_{\rm h}} {\rm d}\chi\, q_{\rm ggm}(\chi)}{\int_0^{\chi_{\rm h}} {\rm d}\chi\, q_{\rm mmg}(\chi)} \frac{\langle\mathcal{N} M_{\rm ap}^2\rangle}{\langle\mathcal{N}^2 M_{\rm ap}\rangle} \frac{\left(R f_{\rm K}^{-1}(\chi_{\rm max})\right)}{\left(R f_{\rm K}^{-1}(\chi_{\rm max})\right)} \tag{45}$$

for a lens sample. We assume here that both kernels $q_{\rm ggm}$ and $q_{\rm mmg}$ peak at the same distance $\chi_{\rm max}$, which is approximately valid for our study. This bias parameters in $r_1/(r_2 b_3)$ are smoothed in k and χ with maximum weight at $k \approx \sqrt{2}/R$ (equilateral triangles) and $\chi_{\rm max}$. The exact smoothing kernels are given in Appendix D. A deviation of $\Psi(R)$ from unity hence indicates a biased galaxy population.

We calculate the $\Psi(R)$ statistics for the samples L1–L6, samples sm1–sm5 and the ETG sample (all low-z only) for angular scales between 1 and 10 arcmin. The remaining measurements are too noisy for useful constraints. Fig. 12 summarizes these novel measurements. The error distributions of the ratios $\Psi(R)$ are estimated by employing Monte Carlo realizations of $\mathcal{B}_{\rm ggm}$ and $\mathcal{B}_{\rm mmg}$ (assumed Gaussian); depicted are the mean and variances σ_Ψ in the resulting distributions. Alternatively, one could utilize the analytic probability distribution function given in Hinkley (1969).

6 DISCUSSION

We performed a G3L analysis of approximately 100 square degrees of the CFHTLenS data set. The data are endowed with photometric redshifts of galaxies and *lensfit* estimates of the PSF-corrected source ellipticities. For the first time, the signal-to-noise ratio of the lensing data is sufficient to measure third-order GGL as a function of lens luminosity, stellar mass and galaxy type. The work of Simon et al. (2008), analysing the RCS1 data, demonstrated that G3L measurements are principally possible with contemporary

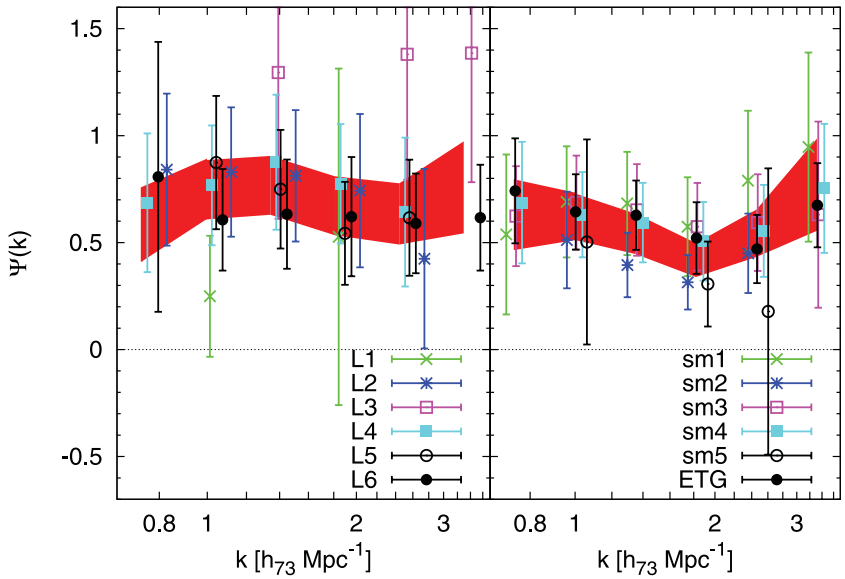

Figure 12. Results of the Ψ-statistics which probes the third-order galaxy biasing parameters of our lens samples. Plotted is $r_1/(b_3 r_2)$ as a function of scale $k = \sqrt{2}/R = \sqrt{2}/(f_K(\chi_{max})\theta)$ for the angular range $1 \leq \theta < 10$ arcmin. Used are only significant measurements in the low-z samples. Luminosity samples are in the left-hand panel, stellar mass samples and the ETG sample in the right-hand panel. The data points with uncertainties larger than $\sigma_\Psi > 0.8$ are not shown. The shaded area indicates the mean and standard deviation of the mean of combined samples. L1–L6: M_r-luminosities increasing from -17.8 mag to -22.4 mag; sm1–sm5: increasing stellar masses from 7×10^9 $M_\odot$ to 10^{11} $M_\odot$; ETG: early-type galaxies.

lensing surveys. This is confirmed by this study. We further subdivided the lens samples in M_r-luminosities, stellar masses, SED types, and a 'low-z' ($0.2 \leq z_{photo} < 0.44$) and a 'high-$z$' ($0.44 \leq z_{photo} < 0.6$) redshift bin by utilizing the photometric redshifts of the lenses. We presented the G3L measurements in terms of aperture statistics that probe the angular bispectrum of the (projected) matter–galaxy three-point correlations. In one case ('lens–lens–shear'), the measurements quantify correlations between two lens positions and the surface matter density around the lens pair; this can be interpreted as excess surface mass density about galaxy pairs (Simon et al. 2012). In the other case ('lens–shear–shear'), it expresses correlations between a lens position and the surface mass density in two different directions close to the lens. The here adopted G3L aperture statistics have the practical advantage to separate E- and B/P-modes from these measurements, which is utilized to detect signatures of possible systematics in the data. On this level, no significant G3L systematics signals were detected.

To reduce the impact due to intrinsic alignments of sources, we separated lens and source galaxy samples physically from each other by exploiting the photometric redshifts in the survey. We showed that in the ideal case of no radial overlap, neither II-correlations nor GI-correlations contribute to the correlator. Owing to the uncertainty in the galaxy redshifts, however, perfectly non-overlapping distributions are hard to achieve. We found that our low-z lens samples have still a small overlap of ∼4 per cent with the source sample, the high-z samples a moderate overlap of ∼12 per cent (overlap of redshift probability distribution functions). Because of the small overlap, at least for the low-z samples we do not expect significant contributions from intrinsic alignment correlations. To test the degree of contamination by GI- and II-correlations, we compared the aperture statistics of the combined sm3–sm5 samples, both low-z ($\bar{z}_d = 0.35$) and high-z ($\bar{z}_d = 0.51$), for two cases. In one case, we selected sources by $0.65 \leq z_{photo} < 1.2$ ($\bar{z}_s = 0.93$) as before. In the second case, we were more conservative by selecting only sources

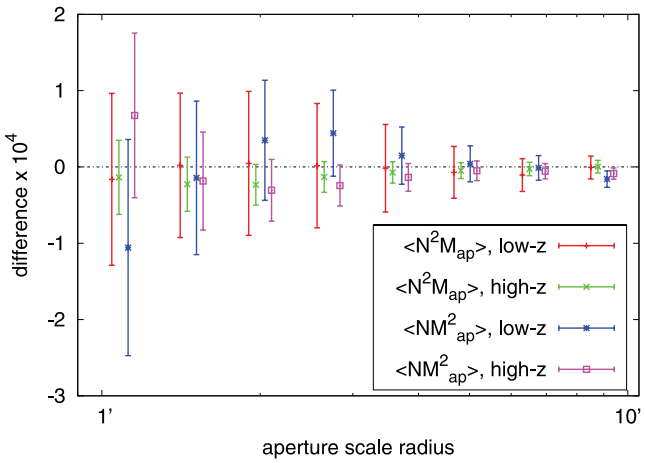

Figure 13. Plotted are the differences of $\langle \mathcal{N}^2 M_{ap}\rangle(\theta)/\int d\chi\, q_{ggm}(\chi)$ for sources with $z_{photo} \geq 0.65$ and $z_{photo} \geq 0.8$ and the analogue for $\langle \mathcal{N} M_{ap}^2\rangle(\theta)/\int d\chi\, q_{mmg}(\chi)$. For fixed lens samples (sm3–5 combined; either low-z or high-z), the result is expected to be consistent with zero. Note that neighbouring error bars are correlated.

within $0.8 \leq z_{photo} < 1.2$ ($\bar{z}_s = 1.02$), thereby discarding about one-third of our sources. However, the latter case reduced the overlap from 3.3 per cent (10.9 per cent) to 0.6 per cent (2.5 per cent) for the low-z (high-z) sample. The statistics were normalized by $\int d\chi q_{ggm}(\chi)$ ($\int d\chi q_{mmg}(\chi)$) to compensate the signal change owing to the different source depths. The maximum signal increase is ∼30 per cent for $\langle \mathcal{N} M_{ap}^2\rangle$ of the high-z lens sample. Fig. 13 shows the difference in normalized statistics for fixed lens samples but varying source depths. Here we assumed that $f_K(\chi_{max})$ is identical for both compared signals, i.e. both signals were differenced at the same aperture scale radius. This assumption is accurate within a few

per cent here. As expected, the difference is consistent with zero, the level of GI/II-systematics in the statistics is therefore negligible within the measurement errors.

As second possible source of systematics, we identified the magnification of the lens number densities by matter fluctuations in front of the lenses. To first-order this effect is comparable to the aperture mass skewness $\langle M_{\rm ap}^3(\theta)\rangle$ associated with sources at redshift $z_{\rm s} \sim 0.4$. We estimated this effect to be of the order of $\lesssim 10^{-8}$ at $\theta \sim 1$ arcmin. We therefore conclude in comparison with our measurements that in the range $1 \lesssim \theta \lesssim 10$ arcmin the lens number density magnification effect is negligible for both $\langle \mathcal{N}^2 M_{\rm ap}\rangle$ and for $\langle \mathcal{N} M_{\rm ap}^2\rangle$. For a more detailed investigation of systematics, however, realistic models of intrinsic alignments and magnification for third-order correlations are required, which are currently unavailable.

The observed aperture statistics depend on the redshift distributions of lenses and sources. Results of the statistics would hence differ when changing the source or lens redshift distribution, even if the underlying comoving spatial 3D matter–galaxy bispectrum was unchanged throughout the light cone. In order to partially correct for this effect, we employed a new technique that normalizes the aperture statistics with the lensing efficiency and relates angular scales to effective spatial scales; this yields two kinds of galaxy–matter bispectra $\mathcal{B}_{\rm ggm}(R)$ and $\mathcal{B}_{\rm mmg}(R)$, originating from $\langle \mathcal{N}^2 M_{\rm ap}\rangle$ and $\langle \mathcal{N} M_{\rm ap}^2\rangle$, respectively. The normalized statistics obtained are basically band bispectra due to the smoothing of the exponential u-filter in k-space and the radial smoothing of the lensing kernels. Only by means of our or similar normalization schemes, measurements for different lens samples or same galaxy selections at different redshifts become comparable. In particular, the application of our normalization simplifies the comparison with results from future studies. The problem of unnormalized measurements becomes particularly obvious for $\langle \mathcal{N}^2 M_{\rm ap}\rangle$ of the low-z L1 sample in Fig. 6 (top left-hand panel) in comparison to the L6 sample in the same panel: for $\theta \gtrsim 2$ arcmin both measurements are basically identical, although the normalization reveals that the lower luminosity galaxies have a smaller bispectrum amplitude (Fig. 11, left-hand panel). This effect results from a completely different redshift distribution of the L1 lenses that, due to sample incompleteness, have a mean redshift of $z \sim 0.22$ instead of L6's $z \sim 0.34$.

We estimated the measurement errors directly from the data by Jackknifing the signal variance across the survey pointings. Ideally, with statistically independent pointings this would properly account for uncertainties due to source shape noise, sampling noise and cosmic variance. However, the pointings are bundled together in large fields W1–W4 with extensions of several degrees across the sky. This makes pointings of the same field partly correlated. Therefore, the cited uncertainties are probably somewhat too optimistic in the sense that they underestimate the cosmic variance.

To refine the previous RCS1 measurement in Simon et al. (2008) for different galaxy populations and to investigate the dependences of bispectra amplitudes on galaxy populations, we focused here on equally sized apertures. This gives most weight to the equilateral bispectra. We found that the aperture statistics are reasonably well described by a power law on angular scales ranging from roughly 2 arcmin to 10 arcmin. On smaller angular scales, we observe evidence for a change of slope, but we are also increasingly affected by the transformation bias. For instance, $\langle \mathcal{N}^2 M_{\rm ap}\rangle$ of the fainter low-z L4 sample clearly flattens below ∼2 arcmin. Qualitatively, this behaviour is also observed in the semi-analytic galaxy models studied in Saghiha et al. (2012), see their fig. 8. A similar change of slope, maybe also a steepening, is visible for the $\langle \mathcal{N} M_{\rm ap}^2\rangle$ statistics of the luminosity samples. A comparison of galaxy models to our measurements requires a careful replication of the galaxy sample selections, their uncertainties and the survey incompleteness. Moreover, as concluded in Saghiha et al. (2012), no reliable galaxy model is currently available to predict the correct amplitude of G3L measurements – or to even double-check whether our results may be strongly effected by galaxy selection effects. We hence postpone this task to a future paper.

Table 4. Values of the normalized galaxy–matter bispectra $\mathcal{B}_{\rm ggm}(R)$ (top half) and $\mathcal{B}_{\rm mmg}(R)$ (bottom half) at $R = 1\,h_{100}^{-1}$ Mpc for the LTG and ETG sample.

Sample	Low-z	High-z
ETG	$+1.04^{+0.17}_{-0.17} \times 10^{-4}$	$+9.48^{+1.19}_{-1.23} \times 10^{-5}$
LTG	$+4.37^{+9.21}_{-5.01} \times 10^{-6}$	$+1.07^{+1.67}_{-1.02} \times 10^{-5}$
ETG	$+5.98^{+1.35}_{-1.41} \times 10^{-5}$	$+1.42^{+1.37}_{-0.92} \times 10^{-5}$
LTG	$+6.93^{+9.91}_{-4.46} \times 10^{-6}$	$-1.39^{+0.95}_{-1.62} \times 10^{-5}$

The measurements of $\mathcal{B}_{\rm ggm}$ utilizing ETG and LTG pairs (subdivision of the combined L5/L6 sample) show that the excess mass around pairs is a strong function of galaxy type. The high excess mass signal of ETG is comparable to the strong signal of pairs in our sm-samples with stellar masses of $\sim 10^{11}$ $\mathrm{M}_\odot$, whereas the excess mass of LTG is consistent with zero in our case (Table 4). A plausible explanation for this is the fact that many ETG in the ETG sample ($\langle M_* \rangle \approx 6 \times 10^{10}$ $\mathrm{M}_\odot$) are satellites in dense cluster environments, whereas LTG are frequently field galaxies. This was, for instance, found by the GGL study of Mandelbaum et al. (2006a) in SDSS. The splitting into ETG from over-dense and under-dense regions that was conducted in this study is actually comparable to the lens–lens–shear correlation function because the G3L correlator gives more weight to pairs in cluster environments, simply because more pairs are found in these regions. Recently, Saghiha et al. (2012) studied the excess mass for two state-of-the-art semi-analytic galaxy models. Although the G3L amplitudes and colour distributions of the two considered models are inconsistent, both models predict a large difference in $\langle \mathcal{N}^2 M_{\rm ap}\rangle$ for $z_{\rm d} = 0.17$ red and blue galaxies up to a factor of $\sim 10^2$ at $\theta \sim 2$ arcmin. With our uncertainties in the LTG signal, we estimate the difference to be at least a factor of ∼10, strongly confirming the previous prediction.

By forming the ratios of normalized bispectra, our new statistic $\Psi(R) := \mathcal{B}_{\rm mmg}(R)/\mathcal{B}_{\rm ggm}(R)$ approximately yields the ratio $r_1/(r_2 b_3)$ of (smoothed) third-order biasing parameters (SW05). The details of the smoothing are determined by the shapes of the u-filter, the peaked kernels $q_{\rm mmg}$, $q_{\rm ggm}$, and to some extent also the matter bispectrum (Appendix D). Deviations of Ψ from unity indicate galaxies that not faithfully trace the underlying matter density field, i.e. biased galaxies. This new technique for investigating galaxy bias with lensing advances the methodology of van Waerbeke (1998) and that of Schneider (1998) that focus on second-order galaxy bias. The application of the latter found that galaxies are generally biased tracers (Hoekstra et al. 2001; Simon et al. 2007; Jullo et al. 2012). We confirm this finding by employing third-order galaxy–matter correlations.

7 CONCLUSIONS

(i) We detect G3L with unprecedented high significance in the CFHTLenS for galaxy populations of different luminosity, stellar mass and SED type. This applies to both third-order

galaxy–galaxy–matter correlations ($\mathcal{B}_{\rm ggm}$) and galaxy–matter–matter correlations ($\mathcal{B}_{\rm mmg}$).

(ii) We find that the (equilateral) galaxy–matter bispectra are, within the remaining statistical errors, reasonably well scale-invariant for the spatial (comoving) scales $0.3 \lesssim k \lesssim 2.2\,{\rm Mpc}^{-1}$. On smaller scales, not included in our power-law fits, there are indications of deviations from the power-law shape in several cases.

(iii) The low-z and high-z counterparts of the same lens samples yield very similar bispectra amplitudes $\mathcal{B}_{\rm ggm}$ (Fig. 11) and slopes (Fig. 9). This points to a little evolution of the bispectrum between redshift $z \sim 0.3$–0.5, especially for our M_r-selected galaxies. There is, however, some evidence for a change in the amplitude of $\mathcal{B}_{\rm ggm}$ for stellar-mass selected galaxies below $\sim 10^{11}\,{\rm M}_\odot$: high-$z$ lenses show a lower amplitude than the low-z lenses (right-hand panel of Fig. 11). This implies an increase of excess mass about pairs of galaxies of fixed stellar mass with time, as, e.g. may be expected in a CDM scenario due to the continuous accretion of matter. The evolution trends of $\mathcal{B}_{\rm mmg}$ are unclear due to the measurement uncertainties in the high-z samples.

(iv) For $\mathcal{B}_{\rm ggm}$, the slope and the amplitude is a changing function of galaxy luminosity, stellar mass and galaxy type. The amplitude change is also observed for $\mathcal{B}_{\rm mmg}$. Brighter or more massive galaxies (by stellar mass) exhibit a steeper bispectrum, which implies that the excess mass is more concentrated in these cases. Moreover, there is a clear trend towards higher amplitudes for both more luminous and more massive galaxies. This shows that more luminous or massive galaxies, or galaxy pairs in the case of $\mathcal{B}_{\rm ggm}$, inhibit denser environments than fainter or lighter galaxies.

(v) We observe a strong signal for the excess mass around ETG pairs. LTG pairs, on the other hand, have a signal that is consistent with zero when studied as aperture statistics. This remarkable observation is in excellent agreement with the recent prediction of Saghiha et al. (2012) based on semi-analytic galaxy models. The measurement therefore suggests that virtually all signal in this magnitude range originates from ETG pairs, and possibly mixed pairs of ETG and LTG, rather than from LTG pairs. This can be explained by the fact that a large fraction of ETG are satellite galaxies in cluster. By explicitly mapping out the excess mass around LTG and ETG galaxy pairs, we have also found that both maps are fundamentally different in their amplitudes as well as in their general appearance.

(vi) The mismatch between $\mathcal{B}_{\rm ggm}$ and $\mathcal{B}_{\rm mmg}$ for the same lens galaxy sample immediately indicates galaxies biased with respect to the matter distribution. This mismatch is captured by the galaxy bias statistics $\Psi(R)$ (Fig. 12) that shows for our low-z samples values comparable for a wide range of galaxy luminosities and stellar masses. Therein, we probe the non-linear regime on scales smaller than $k \sim 0.8\,{\rm Mpc}^{-1}$. We find best constraints on $\Psi(R)$ with the stellar mass samples, which has for all samples sm1–sm5 and scales combined (minimum-variance weighted) an average value of $\overline{\Psi} = 0.51 \pm 0.07$. This shows – for the first time employing third-order lensing statistics – that galaxies are biased tracer of the matter density field. Although $\Psi(R)$ indicates that the ratio $r_1/(r_2 b_3)$ stays relatively constant with scale, with a possible shallow local minimum at $k \approx 1.8\,{\rm Mpc}^{-1}$, the additionally observed change of the bispectrum amplitudes with galaxy luminosity or mass means that the individual bias parameters have to differ between the galaxy samples.

(vii) Finally, we emphasize that theory is lacking behind in interpreting the G3L measurements. Reliable model predictions , e.g. in the vein of Takada & Jain (2003), are needed, not only to properly interpret the measurements, but also to gain a better understanding of systematics and to verify that selection effects in the data do not spoil the measurement.

ACKNOWLEDGEMENTS

We thank Stefan Hilbert for useful discussions and Hananeh Saghiha for verifying our correlator code output with hers on simulated data.

This work is based on observations obtained with MegaPrime/MegaCam, a joint project of CFHT and CEA/IRFU, at the Canada–France–Hawaii Telescope (CFHT) which is operated by the National Research Council (NRC) of Canada, the Institut National des Sciences de l'Univers of the Centre National de la Recherche Scientifique (CNRS) of France and the University of Hawaii. This research used the facilities of the Canadian Astronomy Data Centre operated by the National Research Council of Canada with the support of the Canadian Space Agency. We thank the CFHT staff for successfully conducting the CFHTLS observations and in particular Jean-Charles Cuillandre and Eugene Magnier for the continuous improvement of the instrument calibration and the ELIXIR detrended data that we used. We also thank TERAPIX for the quality assessment and validation of individual exposures during the CFHTLS data acquisition period and Emmanuel Bertin for developing some of the software used in this study. CFHTLenS data processing was made possible thanks to significant computing support from the NSERC Research Tools and Instruments grant programme, and to HPC specialist Ovidiu Toader. The early stages of the CFHTLenS project were made possible thanks to the support of the European Commissions Marie Curie Research Training Network DUEL (MRTN-CT-2006-036133) which directly supported members of the CFHTLenS team (CB, LF, HH, BTPR, PS, MV) between 2007 and 2011 in addition to providing travel support and expenses for team meetings.

TE is supported by the Deutsche Forschungsgemeinschaft through project ER 327/3-1 and, with PS and PS, by the Transregional Collaborative Research Centre TR33 – 'The Dark Universe'. CH, HH and BTPR acknowledge support from the European Research Council under the EC FP7 grant numbers 240185 (CH), 279396 (HH+ES) and 240672 (BR). LVW acknowledges support from the Natural Sciences and Engineering Research Council of Canada (NSERC) and the Canadian Institute for Advanced Research (CIfAR, Cosmology and Gravity programme). HH is supported by the Marie Curie IOF 252760, a CITA National Fellowship and the DFG grant Hi 1495/2-1. HH and ES also acknowledge support from Marie Curie IRG grant 230924 and the Netherlands Organisation for Scientific Research grant number 639.042.814. TDK acknowledges support from a Royal Society University Research Fellowship. YM acknowledges support from CNRS/INSU (Institut National des Sciences de l'Univers) and the Programme National Galaxies et Cosmologie (PNCG). LF acknowledges support from NSFC grants 11103012 and 10878003, Innovation Programme 12ZZ134 and Chen Guang project 10CG46 of SMEC and STCSM grant 11290706600 and Pujiang Programme 12PJ1406700. MJH acknowledges support from the Natural Sciences and Engineering Research Council of Canada (NSERC). TS acknowledges support from NSF through grant AST-0444059-001, SAO through grant GO0-11147A and NWO. MV acknowledges support from the Netherlands Organisation for Scientific Research (NWO) and from the Beecroft Institute for Particle Astrophysics and Cosmology. CB is supported by the Spanish Science Ministry AYA2009-13936 Consolider-Ingenio CSD2007-00060, project 2009SGR1398 from Generalitat de Catalunya and by the European Commissions

Marie Curie Initial Training Network CosmoComp (PITN-GA-2009-238356).

AUTHOR CONTRIBUTIONS

All authors contributed to the development and writing of this paper. The authorship list reflects the lead authors of this paper (P. Simon, T. Erben, and P. Schneider) followed by two alphabetical groups. The first alphabetical group includes key contributors to the science analysis and interpretation in this paper, the founding core team and those whose long-term significant effort produced the final CFHTLenS data product. The second group covers members of the CFHTLenS team who made a significant contribution to either of the project, this paper or both. CH and LVW co-led the CFHTLenS collaboration.

REFERENCES

Bartelmann M., Schneider P., 2001, Phys. Rep., 340, 291
Benitez N., 2000, ApJ, 536, 571
Benjamin J. et al., 2012, MNRAS, submitted (arXiv:1212.3327)
Bernardeau F., van Waerbeke L., Mellier Y., 2003, A&A, 397, 405
Brainerd T., Blandford R. D., Smail I., 1996, ApJ, 466, 623
Chabrier G., 2003, Publ. Astron. Soc. Pac., 115, 763
Cooray A., Sheth R., 2002, Phys. Rev., 372, 1
Crittenden R. G., Natarajan P., Pen U.-L., Theuns T., 2002, ApJ, 568, 20
Dodelson S., 2003, Modern cosmology. Academic Press, Amsterdam
Erben T. et al., 2012, MNRAS, submitted (arXiv:1210.8156)
Erben T. et al., 2009, A&A, 493, 1197
Fischer P. et al., 1999, preprint (arXiv:9912119)
Gladders M. D., Yee H. K. C., 2005, ApJS, 157, 1
Goldberg D. M., Bacon D. J., 2005, ApJ, 619, 741
Goldberg D. M., Natarajan P., 2002, ApJ, 564, 65
Groth E. J., Peebles P. J. E., 1977, ApJ, 217, 385
Hartlap J., Simon P., Schneider P., 2007, A&A, 464, 399
Hetterscheidt M., Simon P., Schirmer M., Hildebrandt H., Schrabback T., Erben T., Schneider P., 2007, A&A, 468, 859
Heymans C., White M., Heavens A., Vale C., van Waerbeke L., 2006, MNRAS, 371, 750
Heymans C. et al., 2012, MNRAS, 427, 146
Heymans C. et al., 2012, MNRAS, submitted
Hildebrandt H., van Waerbeke L., Erben T., 2009, A&A, 507, 683
Hildebrandt H. et al., 2012, MNRAS, 421, 2355
Hinkley D. V., 1969, Biometrika, 56, 635
Hirata C. M., Seljak U., 2004, Phys. Rev. D, 70, 063526
Hoekstra H., Jain B., 2008, Annu. Rev. Nucl. Part. Sci., 58, 99
Hoekstra H., Yee H. K. C., Gladders M. D., 2001, ApJ, 558, L11
Hoekstra H., Van Waerbeke L., Gladders M. D., 2002, ApJ, 577, 604
Hoekstra H., Franx M., Kuijken K., Carlberg R. G., Yee H. K. C., 2003, MNRAS, 340, 609
Hoekstra H., Yee H. K. C., Gladders M. D., 2004, ApJ, 606, 67
Hudson M. J., Gwyn S. D. J., Dahle H., Kaiser N., 1998, ApJ, 503, 531
Jarvis M., Bernstein G., Jain B., 2004, MNRAS, 352, 338
Joachimi B., Mandelbaum R., Abdalla F. B., Bridle S. L., 2011, A&A, 527, A26
Johnston D. E., 2006, MNRAS, 367, 1222
Jullo E. et al., 2012, ApJ, 750, 37
Kaiser N., 1992, ApJ, 388, 272
Kaiser N., Squires G., 1993, ApJ, 404, 441
Kilbinger M., Schneider P., Eifler T., 2006, A&A, 457, 15
Kilbinger M. et al., 2012, MNRAS, in press (arXiv:1212.3338)
Kitching T. D., Miller L., Heymans C. E., van Waerbeke L., Heavens A. F., 2008, MNRAS, 390, 149
Kleinheinrich M. et al., 2006, A&A, 455, 441
Komatsu E. et al., 2011, ApJS, 192, 18
Landy S. D., Szalay A. S., 1993, ApJ, 412, 64
Leauthaud A. et al., 2012, ApJ, 744, 159
Mandelbaum R., Seljak U., Kauffmann G., Hirata C. M., Brinkmann J., 2006a, MNRAS, 368, 715
Mandelbaum R., Hirata C. M., Broderick T., Seljak U., Brinkmann J., 2006b, MNRAS, 370, 1008
Mandelbaum R., Slosar A., Baldauf T., Seljak U., Hirata C. M., Nakajima R., Reyes R., Smith R. E., 2012, preprint (arXiv:1207.1120)
McKay T. A. et al., 2001, preprint (arXiv:0108013)
Meylan G., Jetzer P., North P., Schneider P., Kochanek C. S., Wambsganss J., 2006, in Meylan G., Jetzer P., North P., Schneider P., Kochanek C. S., Wambsganss J., eds, Saas-Fee Advanced Course 33: Gravitational Lensing: Strong, Weak and Micro. Springer: Berlin, p. 552.
Miller L., Kitching T. D., Heymans C., Heavens A. F., van Waerbeke L., 2007, MNRAS, 382, 315
Miller L. et al., 2012, MNRAS, in press (arXiv:1210.8201)
Narayan R., 1989, ApJ, 339, L53
Navarro J. F., Frenk C. S., White S. D. M., 1996, ApJ, 462, 563
Norberg P., Baugh C. M., Gaztañaga E., Croton D. J., 2009, MNRAS, 396, 19
Parker L. C., Hoekstra H., Hudson M. J., van Waerbeke L., Mellier Y., 2007, ApJ, 669, 21
Peacock J. A., 1999, Cosmological Physics. Cambridge Univ. Press, Cambridge
Peebles P. J. E., 1980, The Large-scale Structure of The Universe. Princeton Univ. Press, Princeton, NJ
Pen U.-L., Zhang T., van Waerbeke L., Mellier Y., Zhang P., Dubinski J., 2003, ApJ, 592, 664
Pen U.-L., Lu T., van Waerbeke L., Mellier Y., 2003, MNRAS, 346, 994
Reyes R., Mandelbaum R., Seljak U., Baldauf T., Gunn J. E., Lombriser L., Smith R. E., 2010, Nat, 464, 256
Saghiha H., Hilbert S., Schneider P., Simon P., 2012, A&A, 547, A77
Schneider P., 1998, ApJ, 498, 43
Schneider P., 2003, A&A, 408, 829
Schneider P., 2006, in Meylan G., Jetzer P., North P., Schneider P., Kochanek C. S., Wambsganss J., eds, Saas-Fee Advanced Course 33: Gravitational Lensing: Strong, Weak and Micro Part 3: Weak gravitational lensing. Springer: Berlin, p. 269
Schneider P., Watts P., 2005, A&A, 432, 783 (SW05)
Schneider P., Van Waerbeke L., Jain B., Kruse G., 1998, MNRAS, 296, 873
Schneider P., van Waerbeke L., Mellier Y., 2002, A&A, 389, 729
Schneider P., Kilbinger M., Lombardi M., 2005, A&A, 431, 9
Seljak U., Warren M. S., 2004, MNRAS, 355, 129
Seljak U. et al., 2005, Phys. Rev. D, 71, 043511
Semboloni E., Schrabback T., van Waerbeke L., Vafaei S., Hartlap J., Hilbert S., 2011, MNRAS, 410, 143
Shao J., 1986, Ann. Stat., 14, 1322
Sheldon E. S. et al., 2004, AJ, 127, 2544
Simon P., Hetterscheidt M., Schirmer M., Erben T., Schneider P., Wolf C., Meisenheimer K., 2007, A&A, 461, 861
Simon P., Watts P., Schneider P., Hoekstra H., Gladders M. D., Yee H. K. C., Hsieh B. C., Lin H., 2008, A&A, 479, 655
Simon P., Schneider P., Kübler D., 2012, A&A, 548, 102
Springel V. et al., 2005, Nat, 435, 629
Takada M., Jain B., 2003, MNRAS, 340, 580
Tegmark M., Bromley B. C., 1999, ApJ, 518, L69
van Uitert E., Hoekstra H., Velander M., Gilbank D. G., Gladders M. D., Yee H. K. C., 2011, A&A, 534, 14
van Uitert E., Hoekstra H., Schrabback T., Gilbank D. G., Gladders M. D., Yee H. K. C., 2012, A&A, 545, 71
van Waerbeke L., 1998, A&A, 334, 1
van Waerbeke L., 2010, MNRAS, 401, 2093
Velander M., Kuijken K., Schrabback T., 2011, MNRAS, 412, 2665
Velander M. et al., 2012, MNRAS, submitted
York D. G. et al., 2000, AJ, 120, 1579

APPENDIX A: MULTIPLICATIVE SHEAR BIAS

Miller et al. (2012) discuss a calibration scheme for correlation function estimators involving shear estimates from the *lensfit* pipeline.

For details, we refer the reader to the mentioned article, Section 8.3 and 8.4. Analogous to the calibration scheme of the two-point shear–shear correlation function detailed therein, we divide $\tilde{\mathcal{G}}^{\rm est}$, equation (16), and $\tilde{G}_{\pm}^{\rm est}$, equation (17), by $1 + K_{\mathcal{G}}(\vartheta_1, \vartheta_2, \phi_3)$ and $1 + K_{G_\pm}(\vartheta_1, \vartheta_2, \phi_3)$, respectively. Both calibration factors are given by

$$1 + K_{\mathcal{G}}(\vartheta_1, \vartheta_2, \phi_3) = \frac{\sum_{i=1}^{N_{\rm d}} \sum_{j=1}^{N_{\rm d}} \sum_{k=1}^{N_{\rm s}} w_k (1 + m_k) \Delta_{ijk}^{\vartheta_1 \vartheta_2 \phi_3}}{\sum_{i=1}^{N_{\rm d}} \sum_{j=1}^{N_{\rm d}} \sum_{k=1}^{N_{\rm s}} w_k \Delta_{ijk}^{\vartheta_1 \vartheta_2 \phi_3}} ,$$

$$1 + K_{G_\pm}(\vartheta_1, \vartheta_2, \phi_3) = \frac{\sum_{i=1}^{N_{\rm d}} \sum_{j=1}^{N_{\rm s}} \sum_{k=1}^{N_{\rm s}} w_j w_k (1 + m_j)(1 + m_k) \Delta_{ijk}^{\vartheta_1 \vartheta_2 \phi_3}}{\sum_{i=1}^{N_{\rm d}} \sum_{j=1}^{N_{\rm s}} \sum_{k=1}^{N_{\rm s}} w_j w_k \Delta_{ijk}^{\vartheta_1 \vartheta_2 \phi_3}} . \quad \text{(A1)}$$

The multiplicative bias factors m_i, provided in the CFHTLenS catalogue[3] for each source, are functions of the source signal-to-noise ratio and angular size. Note that for non-vanishing values of $1 + m_i > 0$, the calibration is mathematically equivalent to employing the transformation $\epsilon_i \mapsto \epsilon_i/(1 + m_i)$ and $w_i \mapsto w_i(1 + m_i)$ in the estimators $\tilde{\mathcal{G}}^{\rm est}$ and $\tilde{G}_{\pm}^{\rm est}$.

APPENDIX B: LENS SAMPLES SUPPLEMENT

B1 Angular clustering of lenses

The angular correlation function $\omega(\theta)$ of the lenses as a function of separation θ is approximated by a simple power law (Peebles 1980)

$$\omega(\theta) = A_\omega \left(\frac{\theta}{1\ \text{arcmin}} \right)^{-\lambda} + \text{IC} , \quad \text{(B1)}$$

where A_ω is the clustering strength at a separation of 1 arcmin, λ the slope of the correlation function and the constant offset IC, the integral constraint (Groth & Peebles 1977). We find this fitting function to be a good description of $\omega(\theta)$ between $0\farcm2 \lesssim \theta \lesssim 10$ arcmin. The estimator of $\omega(\theta)$ by Landy & Szalay (1993), employed for this paper, requires the repeated counting of galaxy pairs in separation bins for the random realizations of unclustered galaxy distributions, factoring in the incompleteness of the survey. The figures quoted in Table 1 consider the masks of individual survey pointings, but presuming the same survey completeness within regions that are not masked out. For the final $\omega(\theta)$, all pair counts from all individual survey fields are added so that, in effect, fields with more galaxies attain a higher weight in the average. The binned $\omega(\theta)$ is stored as data vector $\bar{\boldsymbol{d}}$.

Pointing-to-pointing Jackknife sampling to estimate the statistical uncertainty of $\bar{\boldsymbol{d}}$, we prepare a set of $N_{\rm p}$ Jackknife samples $\bar{\boldsymbol{d}}_i^{\rm jn}$, where $\bar{\boldsymbol{d}}_i$ is the combined data vector omitting the ith patch. The Jackknife covariance of the sample mean is then (Shao 1986; Norberg et al. 2009)

$$\mathbf{C} = \frac{1}{N_{\rm p}} \sum_{i=1}^{N_{\rm p}} \Delta\bar{\boldsymbol{d}}_i^{\rm jn} \left[\Delta\bar{\boldsymbol{d}}_i^{\rm jn} \right]^{\rm t} , \quad \text{(B2)}$$

where

$$\Delta\bar{\boldsymbol{d}}_i^{\rm jn} := (N_{\rm p} - 1)(\bar{\boldsymbol{d}} - \bar{\boldsymbol{d}}_i^{\rm jn}) . \quad \text{(B3)}$$

For Table 1, a power-law fit is applied to the ensemble average $\bar{\boldsymbol{d}}$ of all pointings, taking into account the Jackknife covariance $\mathbf{C}$. The θ-binning in $\bar{\boldsymbol{d}}$ is also applied to the power-law model, equation (B1), by averaging the model over the width of each bin. Note that the inverse of $\mathbf{C}$, required for the likelihood analysis of the model fit parameters, has to be corrected to obtain an unbiased estimator of the inverse covariance (Hartlap et al. 2007). Similar corrections of inverse covariances are applied throughout the paper without further mentioning.

B2 Completeness of lens sample

Here, we define a parameter that quantifies the completeness of our lens samples. First, we define the comoving volume $V(z_1, z_2)$ confined by the redshift boundaries $z_1 \le z < z_2$,

$$V(z_1, z_2) = \Omega \int_{\chi(z_0)}^{\chi(z_1)} {\rm d}\chi\ f_{\rm K}^2(\chi) , \quad \text{(B4)}$$

where Ω is the solid angle of the patch field of view minus the solid angle of mask regions, and

$$\chi(z) = D_{\rm H} \int_0^z \frac{{\rm d}z'}{E(z')} , \quad \text{(B5)}$$

where $E(z) := H(z)/H_0$ is the Hubble parameter $H(z)$ as a function of redshift normalized to H_0.

Due to the incompleteness in our flux-limited survey, a galaxy is only visible up to a certain redshift $z_{\rm max}$. In general, and especially for faint galaxies, one can expect the limit $z_{\rm max}$ to be a complicated function of intrinsic galaxy properties and position, survey instrumentation, survey conditions and the data reduction pipeline. Nevertheless, here we take the simplistic view that the main factor is the apparent i'-band magnitude of the lens (extinction corrected), which is limited to $i' \le 22.5$, such that our lens samples are predominantly magnitude limited. We further assume that a K correction is negligible over the redshift bin $[z_1, z_2]$ of interest. Under these circumstances, one finds implicitly for $z_{\rm max}$

$$D_{\rm L}(z_{\rm max}) = 10^{0.4(m_{\rm limit} - m)} D_{\rm L}(z) , \quad \text{(B6)}$$

where z is the redshift of the galaxy, m its i'-band magnitude and $m_{\rm limit} = 22.5$ the asserted magnitude limit of the lens catalogue. By $D_{\rm L}(z) = (1 + z) f_{\rm K}(\chi(z))$, we denote the comoving luminosity distance as a function of redshift.

In order to quantify for Table 1 the completeness of a sample of $N_{\rm g}$ galaxies, we estimate over which fraction $f_{\rm c} = V(z_1, z_{\rm max})/V(z_1, z_2)$ an observed galaxy in the sample would be observable. We take the average of all volume fractions of all lenses in a sample,

$$f_c = \frac{1}{N_{\rm g}} \sum_{i=1}^{N_{\rm g}} \int_{z_1}^{z_2} {\rm d}z\ p_i(z) \frac{V\left(z_1, \text{MIN}(z_{{\rm max},i}; z_2)\right)}{V(z_1, z_2)} , \quad \text{(B7)}$$

and marginalize over the uncertainties in the galaxy redshifts, quantified by the pdf $p_i(z)\,{\rm d}z$. Importantly, $z_{{\rm max},\,i}$ denotes the maximum redshift at which the ith galaxy would still be included within the

[3] Publicly available under http://www.cadc-ccda.hia-iha.nrc-cnrc.gc.ca/community/CFHTLens/query.html

galaxy catalogue, complying with all survey and sample selection criteria. A completeness parameter close to unity means that essentially all galaxies in the sample are visible throughout the entire volume, whereas $f_c \ll 1$ indicates a significant fraction of galaxies that is only visible in a small subvolume at lower redshift. Obviously, f_c is merely an estimator (upper limit) for the sample completeness as galaxies already not observed at redshift z_l are not accounted for. Note that the solid angle Ω cancels inside the expression for f_c and is hence not needed.

APPENDIX C: SYSTEMATICS

C1 B/P-mode consistency with null

As indicator of possible systematics in the estimators, we test $\langle \mathcal{N}^2 M_\perp \rangle$ and the combined $\langle \mathcal{N} M_\perp M_{\rm ap} \rangle$, $\langle \mathcal{N} M_\perp^2 \rangle$ against the null hypothesis. A null measurement should result in

$$\Delta\chi^2 = \boldsymbol{d}^{\rm t} \mathbf{C}^{-1} \boldsymbol{d} \,, \tag{C1}$$

which is statistically consistent with a vanishing signal, with $\boldsymbol{d}$ being a vector consisting of the measurements for the P-mode ($\langle \mathcal{N}^2 M_{\rm ap} \rangle$) or both the P- and B-mode ($\langle \mathcal{N} M_{\rm ap}^2 \rangle$). By $\mathbf{C}$ we denote the Jackknife covariance of the measurements as obtained from the variance of B/P-mode measurements in the pointings, as explained in Section B1. This covariance is larger than a null hypothesis covariance as it possibly also contains power from B/P-modes present in the data. A true null model would contain only power from galaxy shape noise and sampling noise. The test results can be found in Table 2. Measurements inconsistent with a null signal (95 per cent confidence) are underlined, thus for $\Delta\chi^2 \geq 2.0$ (1.68) per degree of freedom for $\langle \mathcal{N}^2 M_{\rm ap} \rangle$ ($\langle \mathcal{N} M_{\rm ap}^2 \rangle$). In total, we find two lens samples that fail the test; they are plotted in comparison to their E-mode in Fig. C1. In both cases the failures are related to the $\langle \mathcal{N} M_{\rm ap}^2 \rangle$ statistics and significantly negative B-modes. Note that errors between neighbouring bins are strongly correlated.

Finding two measurements out of 57 that fail the 95 per cent test is what we would expect as false positive rate. We therefore conclude that the influence of systematics on the E-mode measurement that reveal themselves via the P- or B-modes is likely to be small compared to our measurement uncertainties. Note that the sm7 sample that failed the null test is not used in the final analysis because the corresponding E-mode signal is consistent with zero.

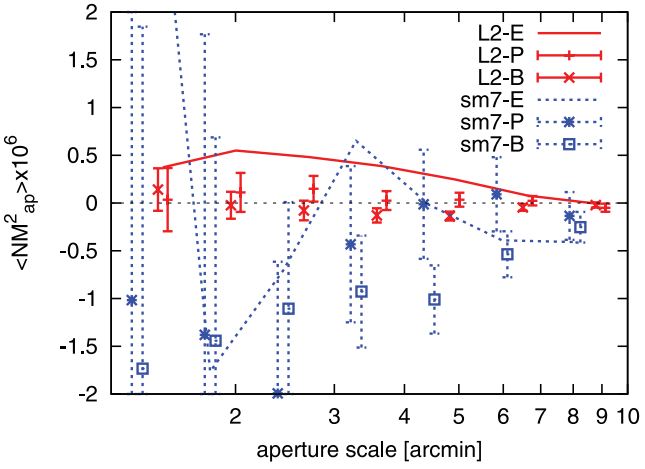

Figure C1. Plots of $\langle \mathcal{N} M_\perp M_{\rm ap} \rangle$, $\langle \mathcal{N} M_\perp^2 \rangle$ (L1 low-z and sm7 high-z) in comparison to the E-mode (lines). Both samples failed the 95 per cent confidence level null test for the P/B-modes, see Table 2.

C2 Field dependence of the G3L signal

The CFHTLS wide survey consists of four contiguous fields W1 (∼72 deg^2), W2 (∼33 deg^2), W3 (∼49 deg^2) and W4 (∼25 deg^2); the field areas do not include masking or excluded fields due to significant PSF residuals. The fields are well separated on the sky and were observed at different times of the year. By splitting the measurements into W1–W4, we check whether the G3L measurements are comparable for different subsets of the data. To have a possibly large sample for this test, we combine the signals of the samples L1 to L6 for each field, see Fig. C2. Only measurements from pointings within the same fields W1–W4 are combined, their statistical uncertainties originate from the Jackknife technique (as in equation B2). Therefore, the error bars do not include the cosmic variance between the fields, which should be most prominent at the larger angular scales.

We find excellent agreement between the measurements, considering that statistical uncertainties at larger scales are higher than indicated and that errors between neighbouring angular bins are correlated. In particular, this separation of data shows that the G3L signal does not originate from singular fields that are extreme outliers compared to the others. Since the uncertainties of the final combined measurements are based on the pointing-to-pointing variance of the entire survey, a possible systematic deviation of one field will be included as systematic error inside the error bars.

APPENDIX D: THIRD-ORDER GALAXY BIASING

The values $\mathcal{B}_{\rm ggm}$ ($\mathcal{B}_{\rm mmg}$) measure the u-filtered bispectrum $\overline{B}_{\rm ggm}$ ($\overline{B}_{\rm mmg}$), radially smoothed with maximum weight at $\chi_{\rm max}$. The maximum weight of the u-filter in Fourier space is at $k = \sqrt{2}/R$ for a given real space scale R. From the definition of the Ψ-statistics, equation (45), from equation (34) and from a similar equation for $\langle \mathcal{N} M_{\rm ap}^2 \rangle$ it follows that

$$\Psi(R) = \frac{\int {\rm d}\chi {\rm d}^2k_1 {\rm d}^2k_2 \, F_{\rm mmg}(\boldsymbol{k}_1, \boldsymbol{k}_2, \chi; R) \, (b_3 r_1)(\boldsymbol{k}_1, \boldsymbol{k}_2, \chi)}{\int {\rm d}\chi {\rm d}^2k_1 {\rm d}^2k_2 \, F_{\rm ggm}(\boldsymbol{k}_1, \boldsymbol{k}_2, \chi; R) \, \left(b_3^2 r_2\right)(\boldsymbol{k}_1, \boldsymbol{k}_2, \chi)} \,,$$

where the smoothing kernels in $\boldsymbol{k}, \chi$-space are

$$F_{\rm mmg}(\boldsymbol{k}_1, \boldsymbol{k}_2, \chi; R) :=$$

$$\frac{q_{\rm mmg}(\chi)}{\int_0^{\chi_{\rm h}} {\rm d}\chi \, q_{\rm mmg}(\chi)} \tilde{u}(k_1\Lambda)\tilde{u}(k_2\Lambda)\tilde{u}(|\boldsymbol{k}_1 + \boldsymbol{k}_2|\Lambda) B_{\rm mmm}(\boldsymbol{k}_1, \boldsymbol{k}_2, \chi),$$

$$F_{\rm ggm}(\boldsymbol{k}_1, \boldsymbol{k}_2, \chi; R) :=$$

$$\frac{q_{\rm ggm}(\chi)}{\int_0^{\chi_{\rm h}} {\rm d}\chi \, q_{\rm ggm}(\chi)} \tilde{u}(k_1\Lambda)\tilde{u}(k_2\Lambda)\tilde{u}(|\boldsymbol{k}_1 + \boldsymbol{k}_2|\Lambda) B_{\rm mmm}(\boldsymbol{k}_1, \boldsymbol{k}_2, \chi) \tag{D2}$$

with $\Lambda := R f_{\rm K}(\chi)/f_{\rm K}(\chi_{\rm max})$. As can be seen, the detailed weight within a band defined by the width of the u-filter is also determined by the actual matter bispectrum $B_{\rm mmm}$.

We can further exploit the statistical isotropy of the galaxy–matter bispectra, which means that both $B_{\rm mmm}$ and the galaxy biasing parameters r_1, r_2, b_3 are only functions of $|\boldsymbol{k}_1|, |\boldsymbol{k}_2|, \phi$; ϕ is the angle spanned by $\boldsymbol{k}_1$ and $\boldsymbol{k}_2$. The previous expressions therefore

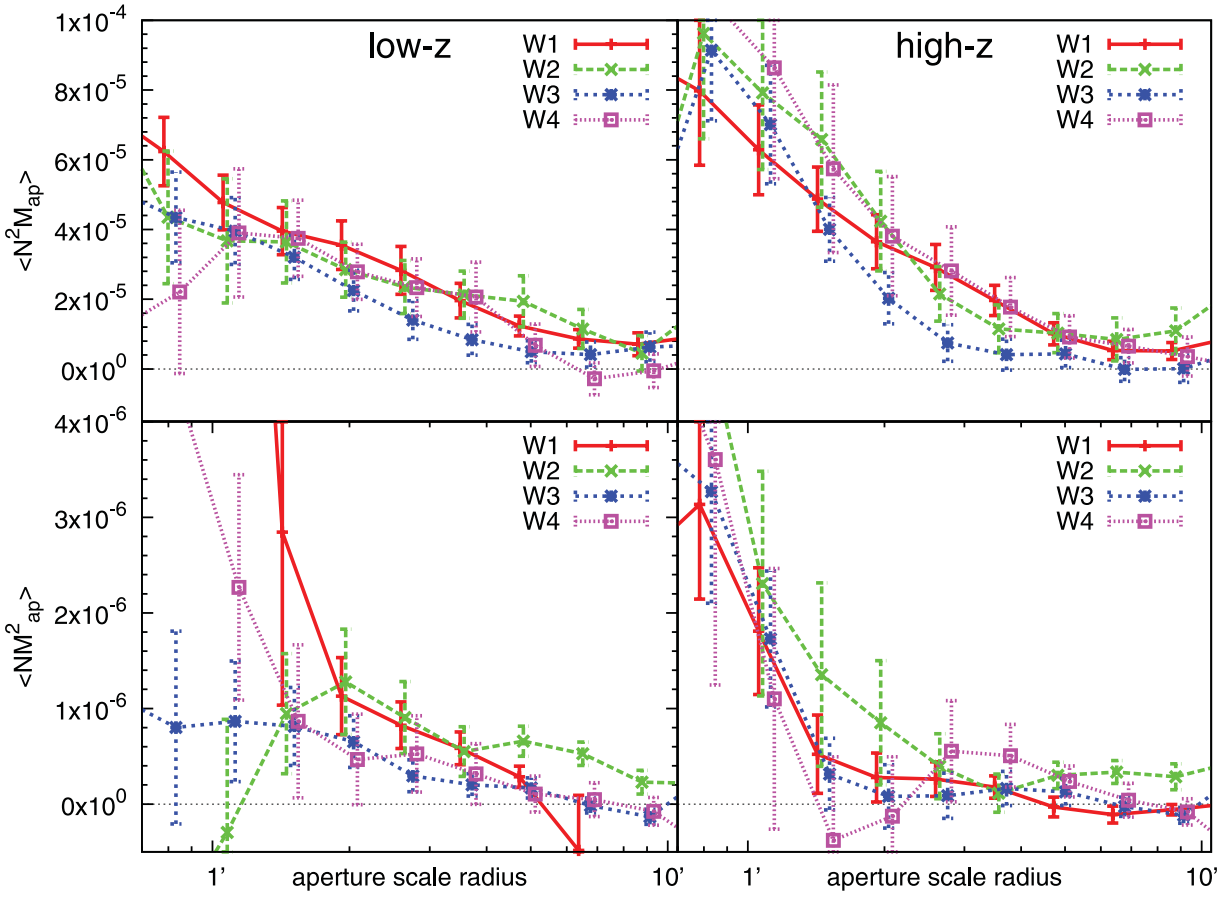

Figure C2. Measurements of the aperture statistics (top row: $\langle \mathcal{N}^2 M_{\rm ap} \rangle$, bottom row: $\langle \mathcal{N} M_{\rm ap}^2 \rangle$) for the combined L1–L6 sample (low-z and high-z redshift bin separately). The measurements are split for the four fields W1–W4. The error bars indicate only the pointing-to-pointing variance within the same field. The fields vary in size and thus the sizes of lens and source catalogues vary. The lines connect the data points to guide the eye.

simplify to

$$\Psi(R) = \frac{\int \mathrm{d}\chi \mathrm{d}\phi\, \mathrm{d}k_1 \mathrm{d}k_2 k_1 k_2\, F_{\rm mmg}(\ldots)\, (b_3 r_1)\, (k_1, k_2, \phi, \chi)}{\int \mathrm{d}\chi \mathrm{d}\phi\, \mathrm{d}k_1 \mathrm{d}k_2 k_1 k_2\, F_{\rm ggm}(\ldots)\, \left(b_3^2 r_2\right)\, (k_1, k_2, \phi, \chi)}\,, \quad \text{(D3)}$$

where

$$F_{\rm mmg}(\ldots) := \frac{q_{\rm mmg}(\chi)}{\int_0^{\chi_{\rm h}} \mathrm{d}\chi\, q_{\rm mmg}(\chi)} \times \tilde{u}(k_1\Lambda)\tilde{u}(k_2\Lambda)\tilde{u}(|\boldsymbol{k}_1 + \boldsymbol{k}_2|\Lambda) B_{\rm mmm}(k_1, k_2, \phi, \chi)\,,$$

$$F_{\rm ggm}(\ldots) := \frac{q_{\rm ggm}(\chi)}{\int_0^{\chi_{\rm h}} \mathrm{d}\chi\, q_{\rm ggm}(\chi)} \times \tilde{u}(k_1\Lambda)\tilde{u}(k_2\Lambda)\tilde{u}(|\boldsymbol{k}_1 + \boldsymbol{k}_2|\Lambda) B_{\rm mmm}(k_1, k_2, \phi, \chi) \quad \text{(D4)}$$

and

$$|\boldsymbol{k}_1 + \boldsymbol{k}_2| = \sqrt{k_1^2 + k_2^2 + 2k_1 k_2 \cos\phi}\,. \quad \text{(D5)}$$

Note that for equilateral triangles we have $k_1 = k_2 = |\boldsymbol{k}_1 + \boldsymbol{k}_2|$ and thus $\cos\phi = -1/2$.

This paper has been typeset from a TEX/LATEX file prepared by the author.